8-20-2015 12:00 AM

Blood Supply to the Brain via the Carotid Arteries: Examining Obstructive and Sclerotic Disorders using Theoretical and Experimental Models

Onaizah Onaizah
The University of Western Ontario

Supervisor
Dr. Mair Zamir
The University of Western Ontario Joint Supervisor
Dr. Tamie Poepping
The University of Western Ontario

Graduate Program in Medical Biophysics
A thesis submitted in partial fulfillment of the requirements for the degree in Master of Science

Blood Supply to the Brain via the Carotid Arteries: Examining Obstructive and Sclerotic Disorders using Theoretical and Experimental Models

(Thesis format: Integrated Article)

by

Onaizah Onaizah

Graduate Program in Medical Biophysics

A thesis submitted in partial fulfillment
of the requirements for the degree of
Master of Science

The School of Graduate and Postdoctoral Studies
The University of Western Ontario
London, Ontario, Canada

Abstract

Stroke remains one of the leading causes of death in North America. Approximately half of all ischemic episodes are a direct result of carotid artery disease, which is a result of both obstructive and sclerotic disorders. Obstructive disease is a result of plaque development that imposes a direct limitation on the physical space available for blood flow. Sclerotic disease involves the hardening of the arteries, as is often a result of aging and disease. While the impact of vessel stiffening is not as obvious, it does interfere with wave propagation. Effects of obstructive and sclerotic disease were studied using a lumped parameter model that was designed to match an experimental in vitro flow loop. Mild to moderate stenosis had minimal impact on blood supply to the brain. Both stiffness of the carotid artery and severe stenosis ($\geq$70%) had a significant reduction on blood supply to the brain ($p<0.01$).

Keywords

Carotid artery disease; carotid stenosis; carotid compliance; impedance; lumped parameter model; atherosclerosis; stroke.

Co-Authorship Statement

This thesis contains materials that have been submitted to peer reviewed journals.

Chapter 2 presents material from an article entitled “Effects of Carotid Artery Disease on Blood Supply to the Brain: Theoretical and Experimental Study,” which has been submitted to *Journal of Biomechanics.* This article is co-authored by Onaizah Onaizah, Tamie L. Poepping, and Mair Zamir. O. Onaizah designed and performed the experiments, analyzed the data, and wrote the manuscript. M. Zamir and T. L. Poepping reviewed the results and edited the manuscript prior to submission.

Acknowledgments

I would like to start off by acknowledging all the wonderful people who have helped me get to this point.

A big shout out to my supervisors who have given me this incredible opportunity. Professor Zamir, thank you for meeting with me every week for the last two years and for always being willing to edit my work. Tamie, thank you for the great conversations that were inspiring and always led to great paths.

I would like to acknowledge my advisory committee members: Dr. David Holdsworth and Dr. Hanif Ladak. Thank you Dr. Ladak, for coming to my seminar even when you had 5 hours of lecture on that fateful day.

My lab members have always been helpful and supportive. Bushra Hussain, thank you for always willing to help and the great advice. Mona Hassanzadeh, for our interesting chats about thesis writing. Amanda DiCarlo for her support and friendship both in and out of the lab. Without you, I never would have been able to do experiments and also wouldn't have had anyone to complain to about those experiments. Michelle Lord, for your friendship and all our ice-cream breaks.

I would also like to acknowledge Hristo Nikolov for the phantom fabrication, and Brian Dalrymple and Frank Van Sas for machining and technical help.

Finally, thank you to my family for their love and support. It was not easy living away from home for the first time but I made it.

Table of Contents

List of Tables

List of Figures

List of Symbols and Abbreviations

CCA – common carotid artery

ICA – internal carotid artery

ECA – external carotid artery

LP – lumped parameter

CT – compliant tube

FR – flow resistor

ID – inner diameter

R – Resistance

C – Compliance

L – Inertance

Z – Impedance

R_{ica} – Resistance of the ICA branch

C_{ica} – Compliance of the ICA branch

L_{ica} – Inertance of the ICA branch

R_{eca} – Resistance of the ECA branch

C_{eca} – Compliance of the ECA branch

L_{eca} – Inertance of the ECA branch

R_{id} – Resistance of the components downstream from the ICA

C_{id} – Compliance of the components downstream from the ICA

L_{id} – Inertance of the components downstream from the ICA

R_{ed} – Resistance of the components downstream from the ECA

C_{ed} – Compliance of the components downstream from the ECA

L_{ed} – Inertance of the components downstream from the ECA

R_0 – Baseline downstream resistance values

C_0 – Baseline downstream compliance values

$D_{stenosis}$ – Inner diameter of the ICA at the stenosis

D_{distal} – Inner diameter of the ICA downstream of the stenosis

$P_{systolic}$ – Systolic pressure

$P_{diastolic}$ – Diastolic pressure

$D_{systolic}$ – CCA inner diameter at systole

$D_{diastolic}$ – CCA inner diameter at diastole

E_p – Peterson's pressure-strain modulus

Re – Reynold's Number

DSA – Digital Subtraction Angiography

CTA – Computed Tomography Angiography

MRA – Magnetic Resonance Angiography

PIV – Particle Image Velocimetry

PTV – Particle Tracking Velocimetry

CFD – Computational Fluid Dynamics

FSI – Fluid Structure Interaction

CEA – Carotid Endarterectomy

WSS – Wall Shear Stress

PDMS – polydimethylsiloxane

PVC – polyvinylchloride

Chapter 1

1 Introduction

This section gives a brief overview of the field and provides the motivation for studying blood flow the brain. The history and evolution of the tools used in this study are presented as well as a brief background on some that are not used in this study but used in the clinic or for research purposes.

1.1 Vascular Disease

1.1.1 Stroke

The World Health Organization defines stroke as an "acute neurologic dysfunction of vascular origin with sudden (within seconds) or at least rapid (within hours) occurrence of symptoms and signs corresponding to the involvement of focal areas in the brain" [1]. It is the result of an interruption in blood supply to the brain or certain regions of the brain [2]. Stroke remains one of the leading causes of death in the world [3]. It is the third leading cause of death in Canada resulting in 14,000 deaths each year [4]. There are an estimated 50,000 strokes in Canada [5] and 700,000 strokes in the United States [6] each year, resulting in a large burden on both the healthcare system (physician services, hospital costs) [7] and the economy (lost wages, decreased productivity, residential care facilities) [8]. About 315,000 Canadians [9] and 4 million Americans [6] are living with the effects of stroke that costs the Canadian economy $3.6 billion dollars each year [8].

Some of the risk factors of stroke are hypertension, diabetes, heart disease, obesity, alcoholism, smoking and genetic factors [1]. Due to increased awareness of modifiable risk factors and better care facilities, the deaths due to stroke are on the decline in the developed world [2, 6]. Stroke is also the leading cause of disability in the United States and Canada and second leading cause of dementia behind Alzheimer's disease [2]. While full recovery from a stroke is possible, it is largely dependent on the extent and location of the brain damagae and 25% of all stroke patients die wihtin the first year [2]. A stroke

often results in depression and weakens the immune system making the patient more vulnerable to infectious diseases [2].

There are two main types of stroke: ischemic and hemorrhagic (Figure 1.1). Ischemic stroke results from a blockage in blood supply to the brain due to a thrombus or emboli. A thrombus is a stationary clot that develops inside a blood vessel whereas an embolus is a clot that typically develops in a larger blood vessel and travels through the bloodstream to block smaller vessels. A cerebral hemorrhage results when a weakened blood vessel or aneurysm bursts resulting in bleeding in the brain. A cerebral hemorrhage is much more likely to result in death (40% result in fatalities) compared to an ischemic stroke; however, it is also far less common [2]. Approximately 85% of all strokes are ischemic in nature [2].

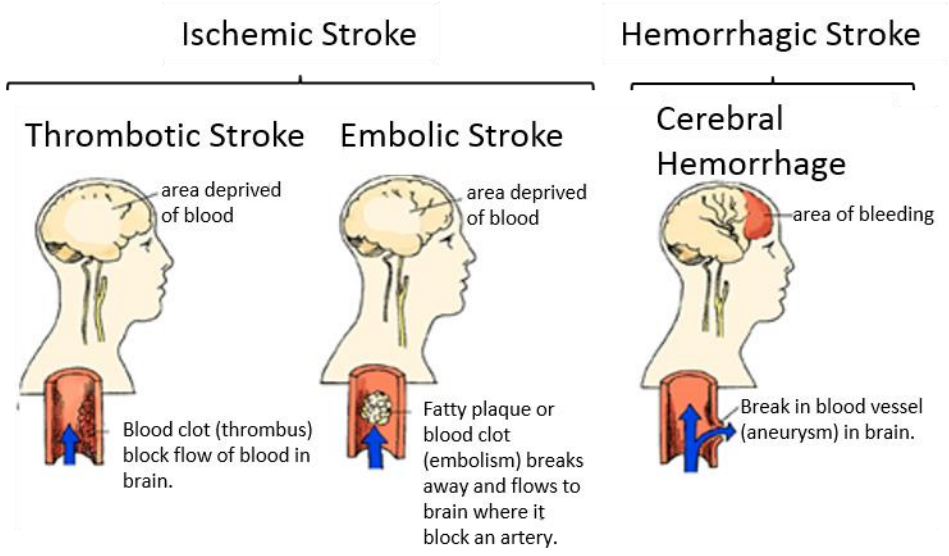

Figure 1.1: Ischemic and hemorrhagic strokes resulting from thrombus, emboli and aneurysms [10].

---

†
Figure 1.1 was adapted from the Nursing Care Plane included in an article posted by Donatello Incognito [10].

1.1.2 Carotid Atherosclerosis

The carotid arteries are major arteries supplying blood to the brain, head and face. The two common carotid arteries (CCAs) located on the left and right side of the neck region branch out from the aorta and the brachiocephalic trunk respectively. The CCA then bifurcates into the internal carotid artery (ICA) and the external carotid artery (ECA). The ICA is a major supply route of blood to the brain while the ECA supplies blood to the head and face (Figure 1.2). In addition, there is also a dilated portion of the vessel located at the bifurcation region and extending into the ICA known as the carotid sinus [11]. The carotid sinus contains baroreceptors that are responsible for checking and maintaining the blood pressure [11].

Atherosclerosis is the narrowing of an artery as a result of plaque development. This is a localized buildup of lipids and cholesterol deposits. Over time, this plaque hardens, resulting in the narrowing of the artery and changing the local blood flow patterns in the region [12]. Atherosclerosis has many of the same risk factors as stroke and because of the nature of the disease; there may not be any signs or symptoms until a stroke occurs [12]. Atherosclerosis often develops in regions with complex flow patterns resulting from complex geometries such as near curvatures and bifurcations [13]. Therefore, the carotid bifurcation due to its geometry is a common site of plaque development.

More than half of all strokes are a direct result of carotid artery disease [14]. Carotid atherosclerosis can lead to an overall reduction in blood supply to the brain [15]. The plaque buildup can get severe enough that it can close the opening to the ICA (occlusion) resulting in a loss of blood flow to a specific region of the brain which could potentially result in a stroke; however, often loss of blood flow from one artery ICA is compensated for by the other side due to the Circle of Willis [15]. The larger problem with plaque development is the potential of emboli formation if the plaque ruptures. The emboli can travel downstream and block the smaller cerebral arteries [16].

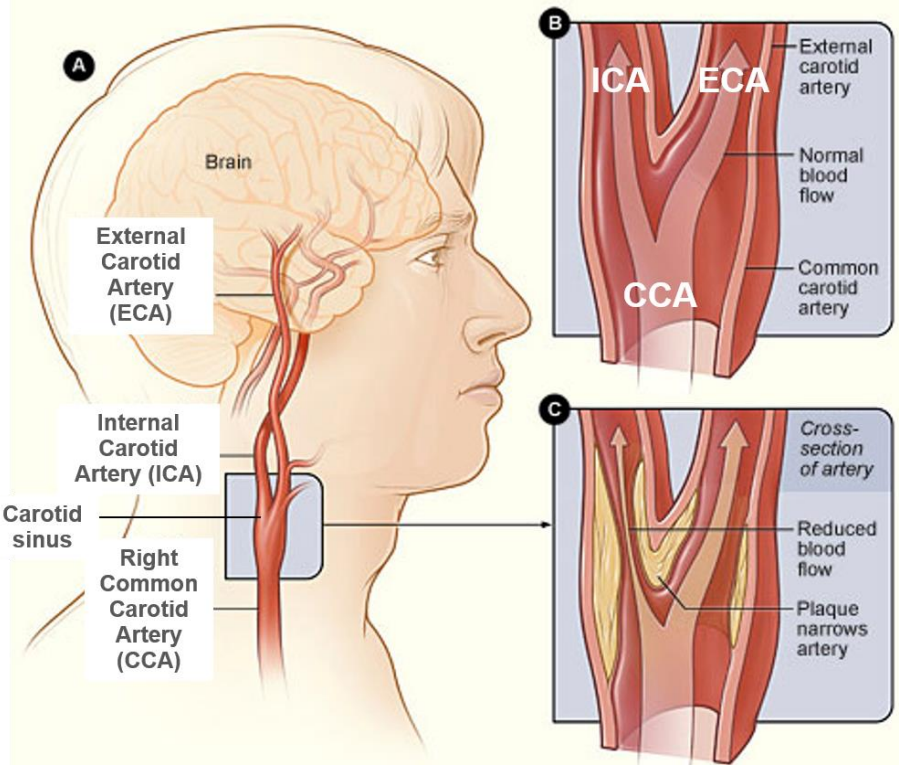

Figure 1.2: (a) The location of the carotid artery as well as its anatomy, (b) blood flow shown through a healthy carotid artery, (c) blood flow through a diseased carotid artery where it is impeded by plaque development [14].

1.1.3 Plaque Geometry, Diagnosis and Treatment

Stenosis severity is the overarching diagnostic measurement tool used to assess the stage and progression of plaque development. Major clinical trials such as the North American Symptomatic Carotid Endarterectomy Trial (NASCET) [17] and the European Carotid Surgery Trial (ECST) [18], have used this measurement. The NASCET trial graded the stenosis based on a diameter reduction by measuring the inner diameter of the stenosis ($D_{stenosis}$) as a percentage of the inner diameter of the downstream ICA (D_{distal}). Stenosis severity as defined in the NASCET trial is shown in Eq. 1.1 and is used as the main predictor of stroke risk.

---

† Figure 1.2 was adapted from the National Heart, Lung and Blood Institute where it was included in the description of carotid artery disease [14].

$$\% \, Stenosis = \left(1 - \frac{D_{stenosis}}{D_{distal}}\right) x100 \qquad 1.1$$

Plaque can form with varying levels of symmetry and it has been shown in several studies that plaque symmetry can influence plaque progression and emboli formation [19-21]. A symmetric or concentric plaque is defined as one that develops equally from all sides of the walls whereas an axisymmetric or eccentric plaque is one that develops more from one side of the wall. Eccentricity influences the local flow patterns and can result in higher shear stress levels and a larger flow division between the ICA and ECA than concentric stenoses [21-24]. Independent of stenosis severity and other risk factors, eccentricity was found to result in increased cerebrovascular events [19].

Ulceration is a morphological feature that results when the surface of the plaque is distorted consisting of a necrotic core [25]. This could be the result of plaque rupture or simply a feature of the plaque formation. The NASCET trial concluded that ulceration is an important risk factor of disease progression and emboli formation as patients with plaque ulceration had a two-year stroke risk of 30% compared to 17% for patients with no ulcerations [26, 27]. In fact, the American Heart Association considers a 50% stenosis with an ulceration to be as severe as a 70% stenosis and recommends equal treatment [27]. In addition, ulceration was found to result in increased downstream flow disturbances and thus an increased risk of stroke [28].

Since large multi-center trials provided strong evidence of the link between carotid plaque and stroke on the symptomatic side, treatment of carotid artery disease is generally recommended for patients with a stenosis severity of 70% or greater, while patients with a stenosis severity of 50% or greater are heavily monitored [17, 18]. Carotid endarterectomy and stenting are the two most common treatments used, and each are described below.

Carotid endarterectomy (CEA) is a surgical technique that involves opening up the carotid artery on the symptomatic side and the physical removal of plaque before the artery is sealed back up. This removal of plaque has been shown to significantly reduce

the risk of cerebrovascular events. CEA remains the gold standard of care for people who are surgically operable and those who request it [29].

Carotid stenting involves placing a stent (mesh) over the region of plaque development inside the artery to stop any further progression of the disease as well as expand the area to allow sufficient flow through the ICA. Multiple trials have shown mixed results for carotid stenting with some showing that CEA reduces the risk of stroke more significantly than stenting [30-32] while others showing that there is no difference in the outcomes [33, 34]. Carotid stenting has been shown to decrease ECA flow due to its placement at the bifurcation [35].

1.1.4 Sclerotic Disease

The ability of the arteries to expand and contract with changes in pressure is an inherent property of blood flow. Sclerotic disease is associated with hardening of the arteries that changes the mechanical properties of the artery walls. Sclerosis is a common result of aging [36-41] but habitual exercise has been found to mitigate these effects [42]. Decrease in compliance can also be caused due to diabetes, heart disease, hypertension, smoking and other risk factors [42]. This loss of compliance is considered to be a predictor of vascular disease as compliance plays a key role in the circulatory homeostasis [42]. The risk of thrombosis, myocardial infarction, aneurysms, and stroke can increase due to a loss of compliance [42].

Compliance is defined as the change in volume over change in pressure ($\frac{\Delta V}{\Delta P}$). However, it is difficult to measure in vivo. Thus, measurements of cross-sectional compliance or elastic modulus are often used [36-41]. This is based on the assumption that changes in diameter with respect to pressure are sufficient to assess the compliance of the arteries as the longitudinal component is considered negligible [36-41]. Peterson's elastic modulus (E_p) is defined as the pressure-strain ratio where the difference between the systolic pressure ($P_{systolic}$) and diastolic pressure ($P_{diastoic}$) is divided by the difference in the systolic inner diameter ($D_{systolic}$) and the diastolic inner diameter ($D_{diastolic}$) of the CCA (Eq. 1.2). K is a factor of 133.32 to convert from units of mmHg to SI units of Pascals.

$$E_p = KD_{diastolic}\left[\frac{P_{systolic} - P_{diastoic}}{D_{systolic} - D_{diastolic}}\right] \quad 1.2$$

To assess arterial compliance of the CCA, data from 6 different studies [36-41] that measured E_p (or provided sufficient information to calculate it) were compiled. In these studies, measurements were made in the carotid arteries using ultrasound imaging techniques to determine the systolic and diastolic inner diameters in the CCA [36-41]. The study then used simultaneous measurements of systolic and diastolic pressure measurements along with the diameter measurements to calculate E_p. The data from these studies are summarized in Figure 1.3, which shows the effects of aging on the elastic modulus. E_p is shown to change drastically between the ages of the 10 and 75 (approximately a factor of 4). While the loss of compliance plays an important role in vascular disease, its impact is not fully understood as it is often neglected in both *in vitro* studies and simulations.

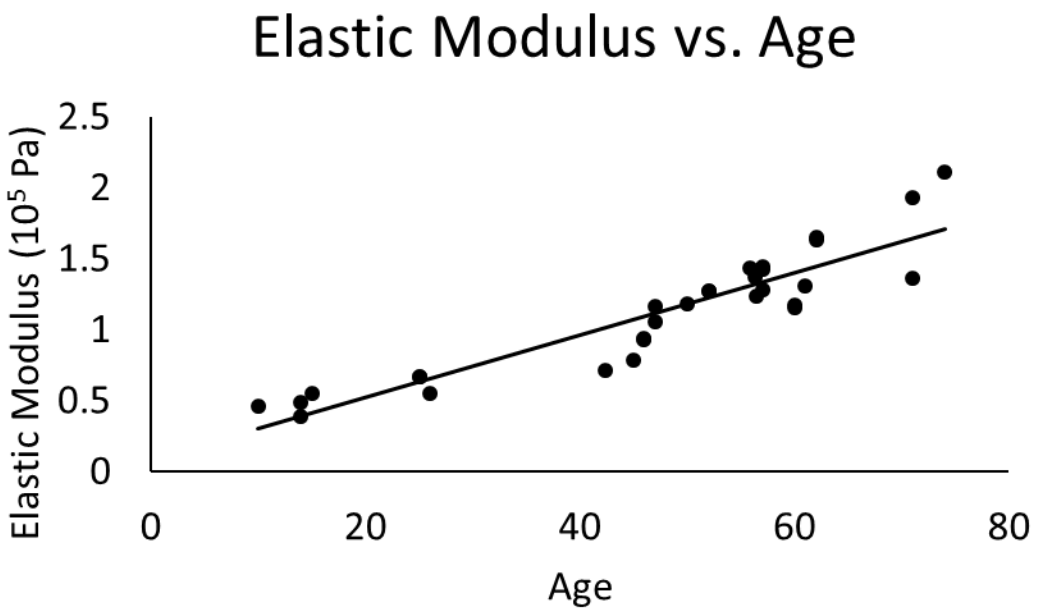

Figure 1.3: Elastic modulus (10^5 Pa) measured for the CCA increases with age. Data are collected from the literature [36-41]. Only the elastic modulus given for normotensive subjects is shown for the study by Laurent et al. (1994) [38].

1.1.5 Carotid Artery Hemodynamics

Hemodynamics plays a key role in the initiation and progression of atherosclerotic plaques [43-46]. The geometry of the carotid bifurcation creates distinctive flow patterns that include recirculation zones with low and oscillating shear stress. This can disrupt the endothelial cells lining the artery and result in plaque formation [47]. This plaque formation can cause disturbed flow, turbulence and regions with high wall shear stress [48, 49].

Both recirculation zones and flow separation have long been considered to play a role in the development of atherosclerotic plaques. The carotid artery is unique in that the dilated portion of the vessel (sinus) consists of a flow separation leading to recirculation zones. Together, these two conditions create an environment susceptible to the development of plaque. Recirculation zones enhance the transport of blood cells to the vessel walls [50-52]. Recirculation zones also favour the development of thrombosis by prolonging the residence time of the thrombogenic material in this bifurcation and sinus region [53].

Disturbed and chaotic flow often results due to the development of atherosclerotic plaques that narrow the artery and bifurcation regions. Consequently, a jet of fluid enters into the internal carotid artery at a high velocity, bounces off the artery ICA walls and results in disturbed flow. Since it does not meet the Reynolds number (Re) criteria (>4000) for turbulence, it is often described as transitional or chaotic flow. While turbulent flow is a form of chaotic flow, a chaotic regime isn't necessarily turbulent and results when small changes in initial conditions lead to major changes in flow patterns. There is, however, a body of literature that suggests that pulsatility can reduce the Re number required for turbulent conditions [23, 54, 55]. Disturbed and turbulent flow have been shown to have high correlation with thrombus formation [56]. Disturbed flow can also cause plaque to rupture and thrombi to mobilize [57]. A measure of turbulence intensity (TI) as applied previously to carotid hemodynamics by Kefayati et al. (2014) [48] is sometimes used to assess random fluctuations in velocities.

Low and oscillating wall shear stress (WSS) at the carotid sinus is responsible for the initial development of atherosclerotic plaques [44, 45]. Progression of these plaques results in narrowing of the artery, which is associated with high shear stress levels [43]. Initially, regions with moderate to high shear stress are protected; however, these higher shear stress levels are located in the same region as the plaques and can cause them to become unstable and eventually to rupture leading to emboli formation [58-61]. Nesbitt et al. (2009) [62] found that when a shear-acceleration zone follows a shear-deceleration zone, thrombosis and cerebrovascular events are more likely to occur. WSS is one of the primary criteria investigated for in vitro studies. However, it is often difficult to quantify with ultrasound therefore it is not used in vivo (or in the clinic).

1.2 Assessment of Carotid Artery Disease and Local Hemodynamics

1.2.1 Geometry and Stiffness

Stenosis severity as defined by the NASCET [17] and ECST [18] trials is used as the primary diagnostic indicator of carotid artery disease. The link between stroke and stenosis severity is well documented. Diagnostic imaging is used in the clinic to quantify stenosis severity for treatment planning. Techniques used to image the geometry of the lumen to detect plaque development include x-ray digital subtraction angiography (DSA), computed tomography angiography (CTA), magnetic resonance angiography (MRA). Measurements made using Doppler ultrasound (DUS) typically give information regarding the local hemodynamics but are used as a surrogate measurement of stenosis severity.

DSA is a fluoroscopy technique that uses an iodinated contrast agent to visualize blood vessels. A pre-contrast image is subtracted from the image with contrast to remove the background and thus illuminate arteries. DSA was used in the NASCET trials when quantifying stenosis severity and for this reason is still considered the gold standard (as recently as 2013) although it is only infrequently used today. DSA has significant restrictions and its accuracy in quantifying the degree of stenosis severity in the NASCET trial was limited especially for stenosis levels greater than 50% where the success rate

was only 48% when compared to surgical specimens [63]. This is because DSA only allows limited views of vessel geometry [64]. Due to the high costs associated with this technique, its invasive nature and complications arising from the contrast agent [65], it has largely been supplanted by other diagnostic techniques such as Doppler ultrasound which has become the most widely used imaging modality.

CTA combines a conventional CT and angiography by using an iodinated contrast agent to visualize blood vessels. Compared to DSA, it is only marginally invasive and can provide high-resolution images of the carotid artery. While the accuracy of single-slice CTA is high for quantifying the degree of stenosis severity, problems do arise with ulcerated plaques [66]. Multiple-detector CTA has had more success in quantifying ulcerated plaques [67]. Some drawbacks to the use of CTA are the high costs associated with it, the radiation exposure from CT itself and complications arising from the use of the contrast agent [68]. For these reasons, CTA is used infrequently and only as a second in line measurement technique if severe stenosis is detected through ultrasonic measurements.

Magnetic Resonance Angiography (MRA) uses a conventional MRI to visualize arteries. In this technique, a contrast agent does not have to be used but gadolinium is often used to enhance the images [69, 70]. Since the contrast agent does not include iodine, complications arising from it are minimal. Black blood MRI techniques also have a high accuracy ($\geq$80%) when quantifying large ulcerated plaques but this drops significantly when it comes to small ulcers (50%) [71]. The main limitations of MRA are the higher costs associated with it, low availability of MR imaging machines in clinical centers as well as the lack of standardization between machines from different manufacturers. MRA is also used only infrequently as a second in line diagnostic tool if severe stenosis are detected through ultrasound; although, some centers are beginning to use MRA more frequently and it is one of the primary research imaging techniques. MRA provides useful information about the plaque composition (significant correlation with histopathology [72]), which has been recognized to play a role in progression of the disease.

Ultrasound imaging is a pulse-echo technique based on the detection of the returning signal from a short pulse sent out at a high frequency. It is the most widely used method for assessing carotid artery stenosis due to its noninvasive nature and relatively low cost. A conventional 2D ultrasound [67, 73], contrast-enhanced ultrasound [74], 3D ultrasound [75], echo-colour Doppler [72] and Doppler ultrasound [76] are all techniques used in the clinic. The accuracy of the technique depends on the degree of stenosis severity with accuracy much higher for stenosis levels below 50% [63]. The main drawback of ultrasound is the high inter- and intra-observer variability that makes its results harder to reproduce and thus reduces its reliability.

Stiffness of the carotid artery is not measured in the clinic and therefore no one diagnostic imaging technique exists. It is only measured for research studies and several large studies such as ARIC (Atherosclerosis Risk in Communities) [39, 40] exist that have quantified the change in CCA inner diameter with systolic and diastolic pressure. The CCA diameters have often been characterized using ultrasound echo-tracking techniques [36-41]. New emerging techniques such as ultrasound [77] and MR elastography [78] (imaging used to map the elastic properties of soft tissue) are now being used for research purposes to quantify the change in CCA diameter over a cardiac cycle.

1.2.2 Hemodynamics

In vivo characterization of local hemodynamics in the carotid artery is done mainly through Doppler Ultrasound (DUS) [76]. Some MR velocimetry techniques [79] are emerging but they remain mainly for research purposes. In vitro characterization of the local hemodynamics at the carotid bifurcation can be done through several laboratory techniques such as particle image velocimetry [48, 49], particle tracking velocimetry [80] and numerical simulations [81, 82].

DUS combines the Doppler effect with ultrasound imaging to characterize the blood flow. When the ultrasound beam is reflected of a moving object (for example: red blood cell), the frequency of the returning echo is shifted relative to the transmitted frequency [76]. This is the Doppler effect as the frequency is directly related to the velocity and

direction of the flow [76]. The measurement of peak systolic velocity through DUS is used to predict the stenosis severity of the carotid artery and is thus used as a substitute measurement of the geometry [76].

PIV (particle image velocimetry) is an optical technique that can be used to obtain the velocity profiles of fluid flows. PIV requires a fluid seeded with tracer particles, where images of the fluid flow are taken in rapid succession separated by a time (Δt). These images can be used to calculate how far a group of particles travels during this time to obtain velocity profiles. PIV is considered the gold standard in flow techniques and has been widely used to assess the local hemodynamics at the carotid bifurcation [48, 49]. While conventional PIV provides 2D information with 2 components of the velocity field, this can be improved by the use of newer techniques such as stereoscopic PIV. This technique is based on the stereoscopic nature of our eyes and is used to provide the third component of the velocity based on depth of field. Furthermore, 3D information can be obtained by stacking multiple planes together. PIV is a non-intrusive technique with high temporal and spatial resolution and thus is a valuable technique when studying hemodynamics [48, 49].

Particle Tracking Velocimetry (PTV) is technique used to track individual particles resident in a fluid compared to PIV where a cluster of particles is grouped together to calculate how far they travel. PTV uses a fluid seeded with particles that is illuminated and the movement of individual particles tracked. Conventional PTV involves a single camera used to obtain 2D information. Similar to PIV, multiple cameras can be used to track particles in 3D. In hemodynamics, PTV is more commonly used in the microvasculature where individual red cells need to be tracked [80] and is not used as often in the larger arteries such as the carotid. Nevertheless, PTV provides valuable information about the flow and can be useful tool when studying plaque initiation as has been demonstrated by tracking particles during numerical simulations [83].

Numerical modelling techniques have emerged as a great tool in the last three decades. Their advantages over experimental techniques are mainly the wide variety of scenarios that can be explored and the minimal costs associated with them.

Computational fluid dynamics (CFD) uses discretization methods such as finite element analysis to obtain numerical solutions to complicated partial differential equations and predict flow patterns. CFD has been used to study vascular flow such as in the case of cerebral aneurysm and the flow patterns surrounding the carotid bifurcation [83]. For the most accurate results, CFD typically employs a geometry that is extracted via in vivo imaging (such as MRI) and is often compared to results obtained via experimental techniques. CFD is able to predict comprehensive velocity profiles of flow within a vessel [76]. CFD does however assume a rigid geometry and elastic properties of the carotid artery are neglected.

Fluid-structure interaction (FSI) is another numerical discretization technique that couples the equations for solid and fluid dynamics. It involves a fluid that interacts with the deformable wall surrounding it. FSI involves a combination of fluid and structural mechanics where the two are modelled to varying levels of complexity. This technique allows the elastic properties of the carotid artery to be accounted for [82].

1.3 Lumped Parameter (LP) Model

Pressure and flow waveforms have specific pulsatile characteristics associated with different regions of the arterial tree [13]. This allows the entire cardiovascular system to be summarized by a lumped parameter (LP) model. The lumped parameter model is an analytical model that is mathematically defined as the electrical analogue of a fluid mechanical system. Eq. 1.3 and Table 1.1 summarize how the hydraulic quantities are related to their electrical analogues. Here, Ohm's Law is shown for the electrical case in Eq. 1.3 where I is current, V is the voltage and Z is the impedance in both the electrical and fluid case. In the fluid case, q is volumetric flow-rate and p is pressure and the two equations are defined for a single frequency as defind by the index n. The arrow shows the electrical abstraction of the fluid system and how the quantities in each are related.

$$I_n = \frac{V_n}{Z_n} \longrightarrow q_n = \frac{p_n}{Z_n} \tag{1.3}$$

Table 1.1: Fluid mechanical properties and how they are used in the lumped model as well as their electrical analogues [84].

Fluid Dynamics	Lumped parameters	Electrical Analogue
Pressure, P	Blood pressure, P	Voltage, V
Volumetric flow rate, Q	Blood flow rate, Q	Current, I
Viscous resistance, R	Viscous resistance, R	Electrical resistance, R
N/A – Compliance used is that of the artery wall not the fluid	Vessel Wall Compliance/Elasticity, C	Capacitance, C
Inertance, L	Blood inertia, L	Inductance, L
Volume, V	Blood volume, V	Charge, q

1.3.1 Components – Resistor, Capacitor, Inductor

A resistor (Figure 1.4) in the electrical setting is used to represent resistance (R) to the flow of electrons (current). In the vascular setting it is used similarly, to represent viscous resistance to blood flow. Since the impedance (Z) of a resistor is not frequency dependent (Eq. 1.4), the ratio of the mean pressure and flow can be used to calculate resistance.

$$Z_R = R \tag{1.4}$$

While the simplest approximation for resistance is Poiseuille's Law with resistance highly dependent on the diameter of the vessel, it is virtually impossible to use in the vascular setting since the vessels are small in length and constantly bifurcating as well as the changing viscous properties due to the shear thinning effect of blood. For this reason, a value of resistance for vascular flow is often derived using the LP model [85].

In an electric circuit, capacitors (Figure 1.4) are used to represent the storage of charge. They consist of two parallel plates separated by a dielectric. When a potential difference occurs, an electric field is generated between them. The capacitor charges up when storage occurs and then at a later time will discharge. Likewise, in an LP model a capacitor is used to represent storage of fluid and thus storage of potential energy. As the main conduit arteries and heart are quite elastic, they tend to store fluid in the different phases of the cardiac cycle. Since the impedance of a capacitor is frequency dependent (Eq. 1.5 – where ω is the angular frequency and C is the compliance), it describes the

relationship between the oscillatory pressure and the oscillatory flow (Eq. 1.6 – where the change in pressure is related to the time integral of the flow) [85].

$$Z_C = \frac{1}{i\omega C} \tag{1.5}$$

$$\Delta P = \frac{1}{C}\int_{t=0} Q dt \tag{1.6}$$

An inductor (Figure 1.4) is an electrical component that resists change in the current flowing through it and stores kinetic energy. In a fluid system, inertance (L) is the equivalent of inductance and used to represent the inertial effects of blood flow. Acceleration and deceleration of fluid flow occurs due to various factors such as vessel geometry, gravity, etc. and therefore results in inertial effects. In fluid flow, devices exist to mimic resistance and compliance in a system whereas inertance is often an unwanted byproduct. The impedance of an inductor is frequency dependent (Eq. 1.7 – where L is the inertance) and connects the pressure drop with oscillatory flow-rate (Eq. 1.8 – where ρ is the density of the fluid and A is the area of the vessel) [85]. The inertance can also result in negative flow during part of the cardiac cycle [85].

$$Z_L = i\omega L \tag{1.7}$$

$$\Delta P = \frac{\rho L}{A}\frac{dQ}{dt} \tag{1.8}$$

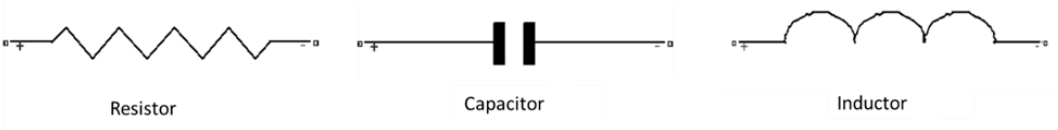

Figure 1.4: Electrical components used in the LP model are shown.

1.3.2 History and Evolution of the LP model

In 1899, Otto Frank mathematically formulated the original LP model or more commonly known as the two-element Windkessel model. This was an electrical circuit designed to model the systemic circulation (pulmonary circulation was neglected). It consisted of a resistor and a capacitor connected in parallel (Figure 1.5a) to describe the storage properties of the large arteries and resistive nature of the small peripheral arteries. It was

based on the reasoning that the diastolic pressure in the descending aorta could be characterized by an exponential curve [85]. While highly sophisticated models have been developed since the introduction of the original two-element model, it is still used today for estimates of arterial compliance. The main drawback of the model is that that it cannot capture high frequency components accurately.

Westerhof et al. (1971) [86] extended the two-element model to include a characteristic impedance (Z_c) that was connected in series to the RC elements (Figure 1.5b). Z_c is defined as ratio of the oscillatory pressure to oscillatory flow. The total resistance (R_T) of the vascular network is now defined as $R + Re(Z_c)$ where R_T is equal to the resistance of the two-element model. The purpose of this three-element Windkessel model was to capture the high frequency components accurately for which it succeeded. Both in vivo and numerical studies have shown that despite its simplicity, the three-element model is good at predicting stroke volume (volume of blood pumped out during each contraction or heart beat), stroke work (work done to eject stroke volume by the heart), and the systolic and diastolic pressures. It does however, underestimate aortic flow and mean arterial pressure and does not provide realistic pressure and flow-rate waveforms since these are dependent on the timing of the forward and reflected pulses.

Both Grant et al. (1987) and Stergiopulos et al. (1999) [87, 88] also extended the three-element model to include an inductor connected in either series or parallel to R_c, respectively (Figure 1.5d-e). The four-element model allowed the inertial effects of blood flow to be accounted and further improved the performance of the model in the low and middle frequency range. Several trials have shown that the model by Grant et al. (1987) [87] most accurately portrays the vascular impedance; however, it is not commonly used as determining values for each parameter becomes difficult due to the number of parameters involved.

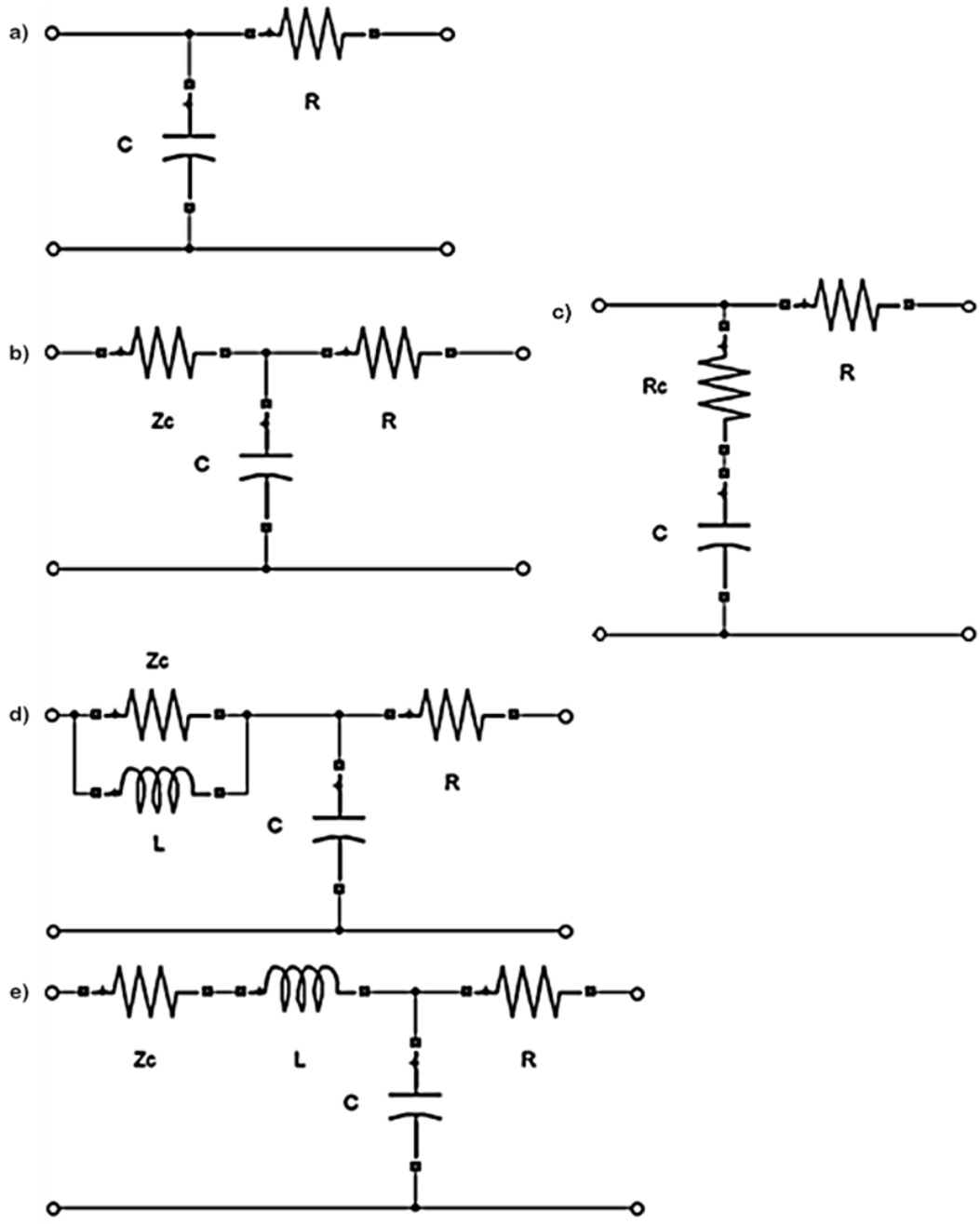

Figure 1.5: Schematic of the different LP models: a) Two-element Windkessel model defined by Otto Frank, b) three-element Windkessel model with characteristic impedance [86], c) viscoelastic model defined by Burattini and Natalucci (1998) [89], d) four-element Windkessel model defined by Stergiopulos et al. (1999) [88], and e) four-element Windkessel model defined by Grant et al. (1987) [87].

Other researchers have worked in parallel in developing different configurations of the LP model. Burattini and Natalucci (1998) [89] developed another configuration of the three-element model where they placed the third component (a resistor) in series with the capacitor to mimic the viscoelastic properties of the artery wall (Figure 1.5c). Huberts et al. (2009) [90] proposed a four-element model where a resistor and inductor were connected in parallel. The purpose of this was to describe the viscous boundary layer encountered at the wall of the artery and flow dominated by inertia in the center of the lumen. While the evolution of the LP model has involved several different applications, a gap does exist in its application to cerebral flow [91] and carotid flow (leading to cerebral and extra-cranial flow).

1.3.3 Advantages and Limitations of the LP Model

While the advantages of numerical modelling have resulted in making some analytical solutions obsolete, the lumped parameter model is still a widely used technique because of its simplicity and lack of computer power required. Lumped parameter models provide reasonable and useful results about the global characteristics of a system. To understand changes in flow and pressure waveforms, an LP model is often used to study the distal impedance of the system. Lumped models have been successfully used for different arteries in the body (typically the aorta) to predict the stroke volume, cardiac output, etc. Some studies have attempted to quantify the arterial impedance of whole body circulation.

An LP model can provide important information about the characteristic impedance of the system. Vascular impedance is an extension of vascular resistance since it provides an important and more complete relationship between pressure and flow [92]. Vascular impedance takes into the account the more dynamic and pulsatile nature of the cardiac flow as well as the elastic nature of the arteries (vascular compliance) and the influences of inertia [91, 93]. Thus, LP models also remain popular because they are commonly used for determining arterial parameters such as arterial compliance. The determination of arterial parameters through waveform analysis remains one of the most frequent

reasons for using a lumped model [94-100]. This is partly due to the fact that these arterial parameters cannot be easily measured or calculated.

The main limitation surrounding the LP model is that it does not account for spatial variations in fluid flow [84]. Because LP models are inherently zero-dimensional (0D), they cannot take into account the 3D nature of the arteries and their impact on the resulting flow patterns [84]. Also, there are various nonlinearities in the system through auto-regulation and neuro-regulation that cannot generally be accounted for with the LP model although sophisticated models have been designed to accommodate this [101].

1.3.4 Previous studies incorporating LP model

The LP model has been used extensively to study the heart with many researchers proposing different models [102-105]. The most popular model [106] remains the elastance model proposed in the 1970's where the left ventricle pressure is defined as a function of the ventricle elastance (inverse of compliance). This model has been adopted by many researchers [103, 107-115] with some groups expanding it to include the Frank-Starling Law [116] (which states that stroke volume increases with increases in the volume of blood into the heart if all other factors remain constant). Other simpler models defined for the heart include the use of an exponential equation to define cardiac output as a function of the atrial pressure [117]. In addition, LP models have been defined to study the heart when ventricular assist devices [115] are present and also models that take the structural and functional properties of the heart valves (preventing backflow) into account [109, 118-120].

More elaborate lumped models have emerged and been applied to specific regions of the arterial tree as well as whole body circulation [96, 121]. The most comprehensive LP model defined by Guyton et al. (1972) [122] was used to account for the interaction between the systemic and pulmonary circulation. In fact, the cardiac output from the left ventricle was mapped all the way back to the right atrium of the heart (known as venous return). Holenstein and Ku (1988) [123] used this approach to find differences in local blood flow patterns between branch points and Eskey et al. (1994) [124] expanded this to tumours. The LP model has been used to study the carotid arteries [125, 126], cerebral

hemodynamics [127], the forearm [128] and for vascular measurements made in animals [88].

The LP model has also been coupled to CFD for various studies as a means of providing boundary conditions [126]. The combined use of these two models allows the characterization of both global and local hemodynamics [126]. As well as accommodating for some of the inherent limitations present in the LP model because CFD offers 3D data that accounts for spatial variation.

Limited work has been done involving both the lumped parameter model and an in vitro carotid artery flow loop although one similar study does exist. Previous work by Kaluzynski et al. (2002) [125] studied arterial input impedance in the carotid artery using an in vitro flow loop containing silicone carotid phantoms. A comparison of two lumped parameter models was done – a ten element model defined for their flow loop with separate branches for the ICA and ECA connected in parallel and a commonly used four-element Windkessel model [87]. Their comparison consisted of goodness of fit measurements between the phase and modulus of the two lumped parameter models with experimental data for a healthy and 90% stenosed phantom. The key difference from our work is that this previous study [125] first defined values of R, L and C, employing various methods that were subsequently used in their fitting. Our study on the other hand outputs the values of R, L and C by iteratively varying them until a best fit is achieved between the experimental and model waveforms.

1.4 Research Objectives, Hypothesis and Thesis Outline

The role of local hemodynamic factors in the carotid artery in the initiation of atherosclerotic plaques and resulting cerebrovascular events is well established and has been the subject of a vast number of studies. On the other hand, while the LP model has existed for more than a 100 years, it has been minimally used to study the carotid arteries and brain vasculature. The goal of this thesis is to study the effects of global parameters such as resistance, compliance and total impedance as well as their impact on the pressure and volumetric flow-rate waveforms.

The overall objectives of this thesis were to: 1) develop a matching LP model to our exiting in vitro flow loop, 2) verify that the LP model provides an accurate representation of the system, 3) study the resulting pressure and volumetric flow-rate waveforms from changes in resistance and compliance, 4) use the LP model to extend our study and make predictions on specific cases for which experimental data were not available (for example: a phantom with physiological compliance could not be built due to manufacturing limitations). These goals were achieved in the study detailed in Chapter 2.

The overall hypothesis of this thesis is that changes resulting due to carotid artery disease and aging impact the lumped parameters (R, C, L), can lead to a reduction in blood supply to the brain and will have a significant impact on the corresponding waveforms. All of these changes can further exacerbate well-established changes in local hemodynamics and increase the risk of a cerebrovascular event.

1.5 References

[1] World Health Organization, *Stroke--1989. Recommendations on stroke prevention, diagnosis, and therapy. Report of the WHO Task Force on Stroke and other Cerebrovascular Disorders.* Stroke, 1989. **20**(10): p. 1407-31.

[2] WebMD - Stroke Health Center. *Understanding Stroke -- The Basics*. 2015 [cited 2015; Available from: http://www.webmd.com/stroke/guide/understanding-stroke-basics.

[3] Domanski, M., et al., *Can we dramatically reduce the incidence of coronary heart disease?* Nat Rev Cardiol, 2011. **8**(12): p. 721-5.

[4] Statistics Canada. *Canada Health Measures Survey – Cholesterol levels of Canadians, 2009-2011*. 2012 [cited 2015; Available from: http://www.statcan.gc.ca/pub/82-625-x/2012001/article/11732-eng.htm.

[5] Hakim, A.M., F. Silver, and C. Hodgson, *Organized stroke care: A new era in stroke prevention and treatment.* Canadian Medical Association Journal, 1998. **159**(6): p. S1.

[6] Hinkle, J.L. and M.M. Guanci, *Acute ischemic stroke review.* J Neurosci Nurs, 2007. **39**(5): p. 285-93, 310.

[7] Canadian Stroke Network. *Quality of Stroke Care in Canada 2011*. 2011 [cited 2015; Available from: http://www.canadianstrokenetwork.ca/wp-content/uploads/2011/06/QoSC-EN1.pdf.

[8] Public Health Agency of Canada. *Tracking Heart Disease and Stroke in Canada, 2009*. 2009 [cited 2015; Available from: http://www.phac-aspc.gc.ca/publicat/2009/cvd-avc/pdf/cvd-avs-2009-eng.pdf.

[9] Public Health Agency of Canada. *Tracking Heart Disease and Stroke in Canada – Stroke Highlights 2011*. 2011 [cited 2015; Available from: http://www.phac-aspc.gc.ca/cd-mc/cvd-mcv/sh-fs-2011/index-eng.php.

[10] Incognito, D.V. *Nursing Care Plan – Cerebrovascular Accident (CVA)*. 2008 [cited 2015; Available from: http://nursingcrib.com/nursing-care-plan/nursing-care-plan-cerebrovascular-accident-cva/.

[11] Cunningham, D.J. and G.J. Romanes, *Cunningham's Textbook of anatomy*. 12th ed. Oxford medical publications1981, London ; New York: Oxford University Press. ix, 1078 p.

[12] WebMD - Heart Disease Health Center. *Carotid Artery Disease: Causes, Symptoms, Tests, and Treatment*. 2015 [cited 2015; Available from: http://www.webmd.com/heart-disease/carotid-artery-disease-causes-symptoms-tests-and-treatment.

[13] Ku, D.N., *Blood flow in arteries.* Annual Review of Fluid Mechanics, 1997. **29**: p. 399-434.

[14] National Heart Lung and Blood Institue. *What is Carotid Artery Disease?* 2010 [cited 2015; Available from: http://www.nhlbi.nih.gov/health/health-topics/topics/catd.

[15] Spencer, M.P. and J.M. Reid, *Quantitation of carotid stenosis with continuous-wave (C-W) Doppler ultrasound.* Stroke, 1979. **10**(3): p. 326-30.

[16] Barnett, H.J., et al., *Causes and severity of ischemic stroke in patients with internal carotid artery stenosis.* JAMA, 2000. **283**(11): p. 1429-36.

[17] North American Symptomatic Carotid Endarterectomy Trial (NASCET) investigators, *Clinical alert: benefit of carotid endarterectomy for patients with high-grade stenosis of the internal carotid artery. National Institute of*

Neurological Disorders and Stroke Stroke and Trauma Division. . Stroke, 1991. **22**(6): p. 816-7.

[18] European Carotid Surgery Trial (ECST) investigators, *Randomised trial of endarterectomy for recently symptomatic carotid stenosis: final results of the MRC European Carotid Surgery Trial (ECST).* Lancet, 1998. **351**(9113): p. 1379-87.

[19] Ohara, T., et al., *Eccentric stenosis of the carotid artery associated with ipsilateral cerebrovascular events.* AJNR Am J Neuroradiol, 2008. **29**(6): p. 1200-3.

[20] Ellis, S., et al., *Morphology of left anterior descending coronary territory lesions as a predictor of anterior myocardial infarction: a CASS Registry Study.* J Am Coll Cardiol, 1989. **13**(7): p. 1481-91.

[21] Tousoulis, D., et al., *Angiographic characteristics of infarct-related and non-infarct-related stenoses in patients in whom stable angina progressed to acute myocardial infarction.* Am Heart J, 1998. **136**(3): p. 382-8.

[22] Tang, D., et al., *Effect of stenosis asymmetry on blood flow and artery compression: a three-dimensional fluid-structure interaction model.* Ann Biomed Eng, 2003. **31**(10): p. 1182-93.

[23] Young, D.F. and F.Y. Tsai, *Flow characteristics in models of arterial stenoses. I. Steady flow.* J Biomech, 1973. **6**(4): p. 395-410.

[24] Long, Q., et al., *Numerical investigation of physiologically realistic pulsatile flow through arterial stenosis.* J Biomech, 2001. **34**(10): p. 1229-42.

[25] Kolodgie, F.D., et al., *Pathology of atherosclerosis and stenting.* Neuroimaging Clin N Am, 2007. **17**(3): p. 285-301, vii.

[26] Eliasziw, M., et al., *Significance of plaque ulceration in symptomatic patients with high-grade carotid stenosis. North American Symptomatic Carotid Endarterectomy Trial.* Stroke, 1994. **25**(2): p. 304-8.

[27] Moore, W.S., et al., *Guidelines for carotid endarterectomy. A multidisciplinary consensus statement from the Ad Hoc Committee, American Heart Association.* Circulation, 1995. **91**(2): p. 566-79.

[28] Wong, E.Y., et al., *Clinical Doppler ultrasound for the assessment of plaque ulceration in the stenosed carotid bifurcation by detection of distal turbulence intensity: a matched model study.* Eur Radiol, 2009. **19**(11): p. 2739-49.

[29] Naylor, A.R., *ICSS and EXACT/CAPTURE: More questions than answers.* Eur J Vasc Endovasc Surg, 2009. **38**(4): p. 397-401.

[30] Ederle, J., et al., *Carotid artery stenting compared with endarterectomy in patients with symptomatic carotid stenosis (International Carotid Stenting Study): an interim analysis of a randomised controlled trial.* Lancet, 2010. **375**(9719): p. 985-97.

[31] Mas, J.L., et al., *Endarterectomy versus stenting in patients with symptomatic severe carotid stenosis.* N Engl J Med, 2006. **355**(16): p. 1660-71.

[32] Mas, J.L., et al., *Endarterectomy Versus Angioplasty in Patients with Symptomatic Severe Carotid Stenosis (EVA-3S) trial: results up to 4 years from a randomised, multicentre trial.* Lancet Neurol, 2008. **7**(10): p. 885-92.

[33] Brott, T.G., et al., *Stenting versus endarterectomy for treatment of carotid-artery stenosis.* N Engl J Med, 2010. **363**(1): p. 11-23.

[34] Forbes, T.L., *Preliminary results of carotid revascularization endarterectomy vs stenting trial (CREST).* J Vasc Surg, 2010. **51**(5): p. 1300-1.

[35] Kabinejadian, F., et al., *Effects of a carotid covered stent with a novel membrane design on the blood flow regime and hemodynamic parameters distribution at the carotid artery bifurcation.* Med Biol Eng Comput, 2015. **53**(2): p. 165-77.

[36] Hansen, F., et al., *Diameter and compliance in the human common carotid artery--variations with age and sex.* Ultrasound Med Biol, 1995. **21**(1): p. 1-9.

[37] Lanne, T., et al., *Differences in mechanical properties of the common carotid artery and abdominal aorta in healthy males.* J Vasc Surg, 1994. **20**(2): p. 218-25.

[38] Laurent, S., et al., *Carotid artery distensibility and distending pressure in hypertensive humans.* Hypertension, 1994. **23**(6 Pt 2): p. 878-83.

[39] Riley, W.A., et al., *Ultrasonic measurement of the elastic modulus of the common carotid artery. The Atherosclerosis Risk in Communities (ARIC) Study.* Stroke, 1992. **23**(7): p. 952-6.

[40] Riley, W.A., et al., *Variation of common carotid artery elasticity with intimal-medial thickness: the ARIC Study. Atherosclerosis Risk in Communities.* Ultrasound Med Biol, 1997. **23**(2): p. 157-64.

[41] Schmidt-Trucksass, A., et al., *Structural, functional, and hemodynamic changes of the common carotid artery with age in male subjects.* Arterioscler Thromb Vasc Biol, 1999. **19**(4): p. 1091-7.

[42] Seals, D.R., *Habitual exercise and the age-associated decline in large artery compliance.* Exerc Sport Sci Rev, 2003. **31**(2): p. 68-72.

[43] Berger, S.A. and L.D. Jou, *Flows in stenotic vessels.* Annual Review of Fluid Mechanics, 2000. **32**: p. 347-382.

[44] Chiu, J.J. and S. Chien, *Effects of disturbed flow on vascular endothelium: pathophysiological basis and clinical perspectives.* Physiol Rev, 2011. **91**(1): p. 327-87.

[45] Davies, P.F., *Hemodynamic shear stress and the endothelium in cardiovascular pathophysiology.* Nat Clin Pract Cardiovasc Med, 2009. **6**(1): p. 16-26.

[46] Giddens, D.P., C.K. Zarins, and S. Glagov, *The role of fluid mechanics in the localization and detection of atherosclerosis.* J Biomech Eng, 1993. **115**(4B): p. 588-94.

[47] Fuster, V., P.M. Steele, and J.H. Chesebro, *Role of platelets and thrombosis in coronary atherosclerotic disease and sudden death.* J Am Coll Cardiol, 1985. **5**(6 Suppl): p. 175B-184B.

[48] Kefayati, S., D.W. Holdsworth, and T.L. Poepping, *Turbulence intensity measurements using particle image velocimetry in diseased carotid artery models: effect of stenosis severity, plaque eccentricity, and ulceration.* J Biomech, 2014. **47**(1): p. 253-63.

[49] Kefayati, S., et al., *In vitro shear stress measurements using particle image velocimetry in a family of carotid artery models: effect of stenosis severity, plaque eccentricity, and ulceration.* PLoS One, 2014. **9**(7): p. e98209.

[50] Affeld, K., et al., *Mathematical model of platelet deposition under flow conditions.* Int J Artif Organs, 2004. **27**(8): p. 699-708.

[51] Muller-Mohnssen, H., *Experimental results to the deposition hypothesis of atherosclerosis.* Thromb Res, 1976. **8**(5): p. 553-66.

[52] Reininger, C.B., et al., *Computational analysis of platelet adhesion and aggregation under stagnation point flow conditions.* Comput Biol Med, 1999. **29**(1): p. 1-18.

[53] Turitto, V.T. and C.L. Hall, *Mechanical factors affecting hemostasis and thrombosis.* Thromb Res, 1998. **92**(6 Suppl 2): p. S25-31.

[54] Young, D.F. and F.Y. Tsai, *Flow characteristics in models of arterial stenoses. II. Unsteady flow.* J Biomech, 1973. **6**(5): p. 547-59.

[55] Sherwin, S.J. and H.M. Blackburn, *Three-dimensional instabilities and transition of steady and pulsatile axisymmetric stenotic flows.* Journal of Fluid Mechanics, 2005. **533**: p. 297-327.

[56] Stein, P.D. and H.N. Sabbah, *Measured turbulence and its effect on thrombus formation.* Circ Res, 1974. **35**(4): p. 608-14.

[57] DePaola, N., et al., *Vascular endothelium responds to fluid shear stress gradients.* Arterioscler Thromb, 1992. **12**(11): p. 1254-7.

[58] Gijsen, F.J., et al., *Strain distribution over plaques in human coronary arteries relates to shear stress.* Am J Physiol Heart Circ Physiol, 2008. **295**(4): p. H1608-14.

[59] Groen, H.C., et al., *Plaque rupture in the carotid artery is localized at the high shear stress region: a case report.* Stroke, 2007. **38**(8): p. 2379-81.

[60] Lovett, J.K. and P.M. Rothwell, *Site of carotid plaque ulceration in relation to direction of blood flow: an angiographic and pathological study.* Cerebrovasc Dis, 2003. **16**(4): p. 369-75.

[61] Slager, C.J., et al., *The role of shear stress in the destabilization of vulnerable plaques and related therapeutic implications.* Nat Clin Pract Cardiovasc Med, 2005. **2**(9): p. 456-64.

[62] Nesbitt, W.S., et al., *A shear gradient-dependent platelet aggregation mechanism drives thrombus formation.* Nat Med, 2009. **15**(6): p. 665-73.

[63] Comerota, A.J., et al., *The preoperative diagnosis of the ulcerated carotid atheroma.* J Vasc Surg, 1990. **11**(4): p. 505-10.

[64] Streifler, J.Y., et al., *Angiographic detection of carotid plaque ulceration. Comparison with surgical observations in a multicenter study. North American Symptomatic Carotid Endarterectomy Trial.* Stroke, 1994. **25**(6): p. 1130-2.

[65] Randoux, B., et al., *Carotid artery stenosis: prospective comparison of CT, three-dimensional gadolinium-enhanced MR, and conventional angiography.* Radiology, 2001. **220**(1): p. 179-85.

[66] Walker, L.J., et al., *Computed tomography angiography for the evaluation of carotid atherosclerotic plaque: correlation with histopathology of endarterectomy specimens.* Stroke, 2002. **33**(4): p. 977-81.

[67] Saba, L., et al., *CT and ultrasound in the study of ulcerated carotid plaque compared with surgical results: potentialities and advantages of multidetector row CT angiography.* AJNR Am J Neuroradiol, 2007. **28**(6): p. 1061-6.

[68] Cinat, M.E., et al., *Computed tomography angiography validates duplex sonographic evaluation of carotid artery stenosis.* Am Surg, 2003. **69**(10): p. 842-7.

[69] Huston, J., 3rd, et al., *Carotid artery: elliptic centric contrast-enhanced MR angiography compared with conventional angiography.* Radiology, 2001. **218**(1): p. 138-43.

[70] Remonda, L., et al., *Contrast-enhanced 3D MR angiography of the carotid artery: comparison with conventional digital subtraction angiography.* AJNR Am J Neuroradiol, 2002. **23**(2): p. 213-9.

[71] Yu, W., et al., *The added value of longitudinal black-blood cardiovascular magnetic resonance angiography in the cross sectional identification of carotid atherosclerotic ulceration.* J Cardiovasc Magn Reson, 2009. **11**: p. 31.

[72] Saba, L., et al., *Imaging of the carotid artery.* Atherosclerosis, 2012. **220**(2): p. 294-309.

[73] Barry, R., C. Pienaar, and C.J. Nel, *Accuracy of B-mode ultrasonography in detecting carotid plaque hemorrhage and ulceration.* Ann Vasc Surg, 1990. **4**(5): p. 466-70.

[74] Magnoni, M., S. Coli, and D. Cianflone, *A surprise behind the dark.* Eur J Echocardiogr, 2009. **10**(7): p. 887-8.

[75] Heliopoulos, J., et al., *Detection of carotid artery plaque ulceration using 3-dimensional ultrasound.* J Neuroimaging, 2011. **21**(2): p. 126-31.

[76] Wong, E., *Hemodynamics in the stenosed carotid bifurcation with plaque ulceration*, in *Department of Medical Biophysics* 2011, Western University: Electronic Thesis and Dissertation Repository.

[77] Zhang, Y.H., Y. Gao, and B.L. Su, *Assessment of Carotid Arterial Wall Elasticity in Type 2 Diabetes Mellitus Patients with Microalbuminuria by Real-Time Ultrasound Elastography.* International Journal of Endocrinology, 2012.

[78] Mariappan, Y.K., K.J. Glaser, and R.L. Ehman, *Magnetic resonance elastography: a review.* Clin Anat, 2010. **23**(5): p. 497-511.

[79] Ku, D.N., et al., *Evaluation of magnetic resonance velocimetry for steady flow.* J Biomech Eng, 1990. **112**(4): p. 464-72.

[80] Omori, T., et al., *Hemodynamics in the microcirculation and in microfluidics.* Ann Biomed Eng, 2015. **43**(1): p. 238-57.

[81] Steinman, D.A., et al., *Reconstruction of carotid bifurcation hemodynamics and wall thickness using computational fluid dynamics and MRI.* Magn Reson Med, 2002. **47**(1): p. 149-59.

[82] Wang, Z., N.B. Wood, and X.Y. Xu, *A viscoelastic fluid-structure interaction model for carotid arteries under pulsatile flow.* Int J Numer Method Biomed Eng, 2015. **31**(5): p. e02709.

[83] Marshall, I., *Targeted particle tracking in computational models of human carotid bifurcations.* J Biomech Eng, 2011. **133**(12): p. 124501.

[84] Kokalari, I., T. Karaja, and M. Guerrisi, *Review on lumped parameter method for modeling the blood flow in systemic arteries* Journal of Biomedical Science and Engineering, 2012. **6**(1): p. 92-99.

[85] Westerhof, N., N. Stergiopulos, and M.I.M. Noble, *Snapshots of hemodynamics : an aid for clinical research and graduate education*. 2nd ed2010, New York: Springer Verlag. xi, 271 p.

[86] Westerhof, N., G. Elzinga, and P. Sipkema, *An artificial arterial system for pumping hearts.* J Appl Physiol, 1971. **31**(5): p. 776-81.

[87] Grant, B.J. and L.J. Paradowski, *Characterization of pulmonary arterial input impedance with lumped parameter models.* Am J Physiol, 1987. **252**(3 Pt 2): p. H585-93.

[88] Stergiopulos, N., B.E. Westerhof, and N. Westerhof, *Total arterial inertance as the fourth element of the windkessel model.* American Journal of Physiology-Heart and Circulatory Physiology, 1999. **276**(1): p. H81-H88.

[89] Burattini, R. and S. Natalucci, *Complex and frequency-dependent compliance of viscoelastic windkessel resolves contradictions in elastic windkessels.* Med Eng Phys, 1998. **20**(7): p. 502-14.

[90] Huberts, W., E.M. Bosboom, and F.N. van de Vosse, *A lumped model for blood flow and pressure in the systemic arteries based on an approximate velocity profile function.* Math Biosci Eng, 2009. **6**(1): p. 27-40.

[91] Zhu, Y.S., et al., *Increases in cerebrovascular impedance in older adults.* J Appl Physiol (1985), 2011. **111**(2): p. 376-81.

[92] Tzeng, Y.C. and G.S. Chan, *Unraveling the human cerebral circulation: insights from cerebral blood pressure and flow recordings.* J Appl Physiol (1985), 2011. **111**(2): p. 349-50.

[93] Zamir, M., *The physics of coronary blood flow*. Biological and medical physics, biomedical engineering2005, New York: Springer. xvii, 408 p.

[94] Diourte, B., et al., *Study of arterial blood pressure by a Windkessel-type model: influence of arterial functional properties.* Computer Methods and Programs in Biomedicine, 1999. **60**(1): p. 11-22.

[95] Laskey, W.K., et al., *Estimation of Total Systemic Arterial Compliance in Humans.* Journal of Applied Physiology, 1990. **69**(1): p. 112-119.

[96] Liang, F.Y. and H. Liu, *A closed-loop lumped parameter computational model for human cardiovascular system.* Jsme International Journal Series C-Mechanical Systems Machine Elements and Manufacturing, 2005. **48**(4): p. 484-493.

[97] Liu, Z.R., K.P. Brin, and F.C.P. Yin, *Estimation of Total Arterial Compliance - an Improved Method and Evaluation of Current Methods.* American Journal of Physiology, 1986. **251**(3): p. H588-H600.

[98] Randall, O.S., et al., *Arterial Compliance in Hypertension.* Australian and New Zealand Journal of Medicine, 1976. **6**: p. 49-59.

[99] Stergiopulos, N., J.J. Meister, and N. Westerhof, *Simple and Accurate Way for Estimating Total and Segmental Arterial Compliance - the Pulse Pressure Method.* Ann Biomed Eng, 1994. **22**(4): p. 392-397.

[100] Stergiopulos, N., J.J. Meister, and N. Westerhof, *Evaluation of methods for estimation of total arterial compliance.* Am J Physiol, 1995. **268**(4 Pt 2): p. H1540-8.

[101] Shi, Y., *Lumped-Parameter Modelling of Cardiovascular system Dynamics under different healthy and diseased conditions*, in *Department of Cardiovascular Science*2013, University of Sheffield.

[102] Cavalcanti, S. and E. Belardinelli, *Modeling of cardiovascular variability using a differential delay equation.* Ieee Transactions on Biomedical Engineering, 1996. **43**(10): p. 982-989.

[103] Lu, K., et al., *A human cardiopulmonary system model applied to the analysis of the Valsalva maneuver.* American Journal of Physiology-Heart and Circulatory Physiology, 2001. **281**(6): p. H2661-H2679.

[104] Sun, Y., et al., *A comprehensive model for right-left heart interaction under the influence of pericardium and baroreflex.* American Journal of Physiology-Heart and Circulatory Physiology, 1997. **272**(3): p. H1499-H1515.

[105] Ursino, M., *Interaction between carotid baroregulation and the pulsating heart: a mathematical model.* American Journal of Physiology-Heart and Circulatory Physiology, 1998. **275**(5): p. H1733-H1747.

[106] Suga, H., K. Sagawa, and A.A. Shoukas, *Load independence of the instantaneous pressure-volume ratio of the canine left ventricle and effects of epinephrine and heart rate on the ratio.* Circ Res, 1973. **32**(3): p. 314-22.

[107] Barnea, O., et al., *Cardiac energy considerations during intraaortic balloon pumping.* IEEE Trans Biomed Eng, 1990. **37**(2): p. 170-81.

[108] Beyar, R., et al., *Interaction between cardiac chambers and thoracic pressure in intact circulation.* Am J Physiol, 1987. **253**(5 Pt 2): p. H1240-52.

[109] Pennati, G., et al., *A mathematical model of circulation in the presence of the bidirectional cavopulmonary anastomosis in children with a univentricular heart.* Med Eng Phys, 1997. **19**(3): p. 223-34.

[110] Migliavacca, F., et al., *Modeling of the Norwood circulation: effects of shunt size, vascular resistances, and heart rate.* Am J Physiol Heart Circ Physiol, 2001. **280**(5): p. H2076-86.

[111] Pennati, G., M. Bellotti, and R. Fumero, *Mathematical modelling of the human foetal cardiovascular system based on Doppler ultrasound data*. Med Eng Phys, 1997. **19**(4): p. 327-35.

[112] Santamore, W.P. and D. Burkhoff, *Hemodynamic consequences of ventricular interaction as assessed by model analysis.* Am J Physiol, 1991. **260**(1 Pt 2): p. H146-57.

[113] Ursino, M., A. Fiorenzi, and E. Belardinelli, *The role of pressure pulsatility in the carotid baroreflex control: a computer simulation study.* Comput Biol Med, 1996. **26**(4): p. 297-314.

[114] Ursino, M., *A mathematical model of the carotid baroregulation in pulsating conditions.* IEEE Trans Biomed Eng, 1999. **46**(4): p. 382-92.

[115] Yaku, H., et al., *Multicompartment model for mechanics and energetics of fibrillating ventricle.* Am J Physiol, 1991. **260**(1 Pt 2): p. H292-9.

[116] Werner, J., D. Bohringer, and M. Hexamer, *Simulation and prediction of cardiotherapeutical phenomena from a pulsatile model coupled to the Guyton circulatory model.* IEEE Trans Biomed Eng, 2002. **49**(5): p. 430-9.

[117] Cavalcanti, S. and L.Y. Di Marco, *Numerical simulation of the hemodynamic response to hemodialysis-induced hypovolemia.* Artif Organs, 1999. **23**(12): p. 1063-73.

[118] Drzewiecki, G., et al., *Modeling of mechanical dysfunction in regional stunned myocardium of the left ventricle.* IEEE Trans Biomed Eng, 1996. **43**(12): p. 1151-63.

[119] Heldt, T., et al., *Computational modeling of cardiovascular response to orthostatic stress.* J Appl Physiol (1985), 2002. **92**(3): p. 1239-54.

[120] Vollkron, M., et al., *Interaction of the cardiovascular system with an implanted rotary assist device: simulation study with a refined computer model.* Artif Organs, 2002. **26**(4): p. 349-59.

[121] Snyder, M.F., V.C. Rideout, and R.J. Hillestad, *Computer modeling of the human systemic arterial tree.* J Biomech, 1968. **1**(4): p. 341-53.

[122] Guyton, A.C., T.G. Coleman, and H.J. Granger, *Circulation: overall regulation.* Annu Rev Physiol, 1972. **34**: p. 13-46.

[123] Holenstein, R. and D.N. Ku, *Reverse Flow in the Major Infrarenal Vessels - a Capacitive Phenomenon.* Biorheology, 1988. **25**(6): p. 835-842.

[124] Eskey, C.J., et al., *Residence Time Distributions of Various Tracers in Tumors - Implications for Drug-Delivery and Blood-Flow Measurement.* Journal of the National Cancer Institute, 1994. **86**(4): p. 293-299.

[125] Kaluzynski, K., et al., *Studies of Arterial Input Impedance in Models of Carotid Artery.* Journal of Mechanics in Medicine and Biology, 2003. **3**(1): p. 9-19.

[126] Urquiza, S.A., et al., *Multidimensional modelling for the carotid artery blood flow.* Computer Methods in Applied Mechanics and Engineering, 2006. **195**(33-36): p. 4002-4017.

[127] Chan, G.S., et al., *Contribution of arterial Windkessel in low-frequency cerebral hemodynamics during transient changes in blood pressure.* J Appl Physiol (1985), 2011. **110**(4): p. 917-25.

[128] Nielson, C.A., et al., *Impact of a smoking cessation lifestyle intervention on vascular mechanics in young women.* Applied Physiology Nutrition and Metabolism-Physiologie Appliquee Nutrition Et Metabolisme, 2014. **39**(5): p. 572-580.

Chapter 2

2 Effects of Carotid Artery Disease on Blood Supply to the Brain: Theoretical and Experimental Study

2.1 Introduction

The carotid artery is one of the major supply routes for blood supply to the brain [1]. Uninterrupted blood flow from the aortic arch to the brain via the common carotid artery, carotid sinus, and internal carotid artery is therefore the subject of much clinical monitoring and concern [2-3]. Stroke resulting from ischemic episodes or thrombotic events within the brain remains a leading cause of death in North America [4]. In both cases there is a disruption in blood flow to the brain. There has been a considerable body of theoretical and experimental work aimed at studying the nature of hemodynamic disruptions that may occur as a result of disease within the carotid artery or sinus [5-14]. However, the major focus of these studies has been on *local* hemodynamic changes, or in the case of clinical studies, the focus has been largely on the *local* pathology (e.g. plaque composition). The ultimate effects of these local disruptions, as well as more general changes to resistance and compliance, on blood supply to the brain remains unclear. The present study was designed to address this issue.

We consider two types of changes within the carotid arteries that may lead to hemodynamic disruptions: obstructive changes, leading to a direct reduction in the physical space available to the flow, and sclerotic changes affecting the mechanical properties of the arterial wall. The difference between the two is important both clinically because of the different pathologies that may lead to these changes, and hemodynamically because of the different consequences for blood supply to the brain that may result from these changes. More specifically, obstructive changes may result from atherosclerotic plaques [1] and may lead to an increase in (local) resistance to flow, while

---

*
A version of this chapter has been submitted to *Journal of Biomechanics* as an original article entitled "Effects of Carotid Artery Disease on Blood Supply to the Brain: A Theoretical and Experimental Study" by O. Onaizah, T. L. Poepping and M. Zamir.

sclerotic changes (either local or global) may result from arteriosclerosis associated with disease or aging [15] and may lead to a disruption in the pulsatile dynamics of the flow.

We used two parallel avenues to extrapolate from local changes within the carotid arteries to global consequences on blood flow to the brain: an experimental setup, with a physiologically based phantom of the carotid arteries and sinus coupled with physiologically based resistance and compliance components downstream, [6, 16] and a theoretical lumped parameter (LP) model [17-20] that allowed us to verify and extend the results beyond the parameter values available in the experiment. Only limited work on blood flow to the brain via the carotid arteries has been done in the past using this methodology [21]. The aim of our study was to establish a method of assessing the significance of pathologies within the carotid arteries and downstream vasculature, not in terms of the severity of these pathologies, but in terms of their ultimate effects on blood supply to the brain.

2.2 Methods

2.2.1 Experimental Setup

An in vitro flow loop, as previously described, [6, 22] consisted of life-size carotid artery bifurcation phantoms of varying geometry and compliance (Figure 2.1), downstream resistance and compliance components, and a programmable positive-displacement pump [23] (CompuFlow 1000, Shelley Medical Imaging, London CAN). A Newtonian blood-mimicking-fluid (BMF) with suitable dynamic viscosity of 4.31 ± 0.03 mPa.s was used [24].

The study incorporates a family of carotid artery bifurcation phantoms starting with normal (disease-free) geometry and progressing to eccentric 30%, 50%, 70% stenosis of the internal carotid artery (ICA) based on diameter reduction relative to the downstream ICA (NASCET criteria) [25-26]. The phantoms were manufactured from polydimethylsiloxane (PDMS) (Sylgard 184, Dow Corning) using a lost-material method to create a low-compliance version with a hollow flow channel in a block of PDMS (Figure 2.1b). Also, for the 50%-stenosed geometry, an additional, more compliant

phantom - consisting of a vessel with 1-mm thick PDMS wall mounted in a box - was studied (Figure 2.1c).

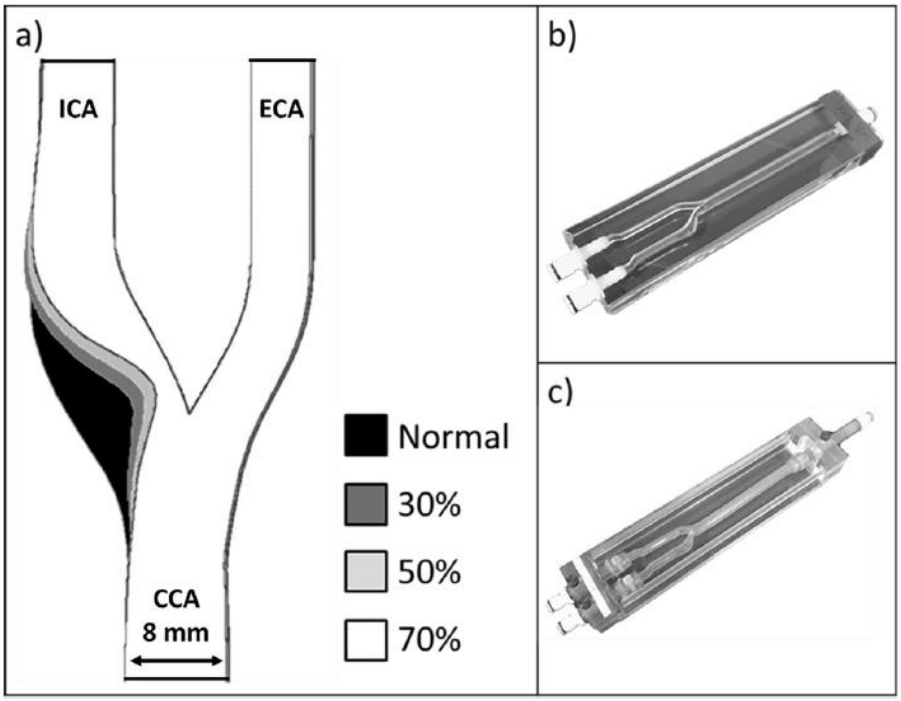

Figure 2.1: (a) Family of phantom geometries with increasing plaque progression (stenosis severity) overlaid on the normal (plaque-free) geometry. (b) Rigid phantom consisting of a hollow flow channel in a PDMS (polydimethylsiloxane) block. (c) Compliant phantom consisting of PDMS vessel with 1-mm thick walls mounted inside an acrylic box.

A schematic of the full in vitro flow loop is shown in Figure 2.2a. Upstream tubing consisted of a 50-cm length of 6.5-mm inner diameter (ID) rigid polyvinylchloride (PVC) tubing. In-line electromagnetic flow-meter probes (EP625/620, Carolina Medical Electronics) were inserted upstream of the common carotid artery (CCA) and downstream of the ICA and external carotid artery (ECA). Custom-built flow-meter sections included a hemostasis valve for inserting a pressure catheter (SPR 350S, size 5F, Millar Instruments, Inc., Houston, TX), which thus enabled simultaneous measurements of pressure and volumetric flow-rate waveforms (sampling rate of 1 kHz). Downstream components were implemented to simulate the in vivo vascular bed. A 30-

cm length of compliant tubing section (CT in Figure 2.2) (9.6-mm ID C-Flex tubing 06424-12, Cole-Parmer) was followed by 1.80 ± 0.25 mm ID flow resistors (FR in Figure 2.2) (Silastic Laboratory tubing, Dow Corning), and 1-m length of rigid PVC tubing (6.5 mm ID, Clearbraid K3150-04, Kuri Tec) before returning to the pump reservoir. The ECA flow resistor (30 cm) was twice as long as for the ICA (15 cm) to produce a 2:1 ICA-to-ECA flow division (an average over the cardiac cycle), approximating in vivo conditions [27]. In order to determine the properties of the downstream components, separate experiments were performed with reduced flow loops that did not include the carotid phantom (Figure 2.2b) as described under Experimental Protocol.

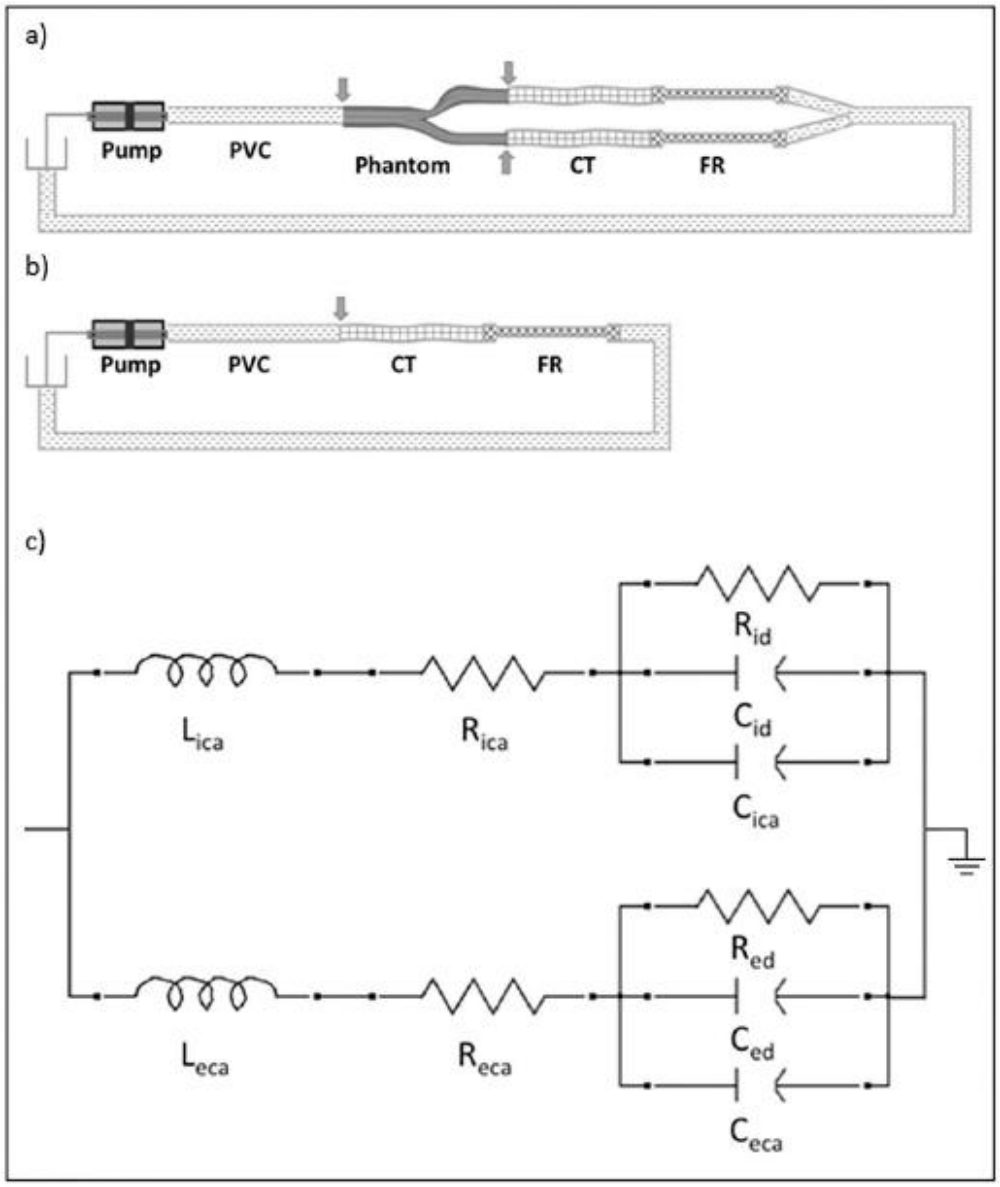

Figure 2.2: (a) Schematic of in vitro flow loop incorporating phantom based on in vivo carotid geometry with downstream compliant tubing (CT) and flow resistors (FR) to mimic downstream vasculature. Pressure and flow waveforms were measured at locations indicated by arrows. (b) Reduced flow loop used to determine the parameter values of downstream elements. (c) LP model used an analogue of the in vitro flow loop. Resistance (R), compliance (C), and inertance (L) were placed as shown for different parts of the flow loop, with subscripts 'ica', 'eca' referring to ICA and ECA branches of the phantom and 'id', 'ed' referring to corresponding downstream elements.

The pump was programmed to deliver one of two CCA flow-rate waveforms: one representing young healthy adults [28] and the other representing older adults with little to no carotid artery disease, [27] as shown in Figure 2.3, along with their frequency content. The "young" waveform was based on Doppler ultrasound peak-velocity waveforms, recorded in the common carotid of 17 healthy volunteers aged 28 ± 3 years used to analytically derive a corresponding flow-rate waveform (mean 6.0 mL/s, Figure 2.3a) [28]. The "old" waveform was based on retrospectively gated phase-contrast MRI used to obtain volumetric flow rate in 94 subjects aged 68 ± 8 years with little or no carotid artery disease, to obtain a characteristic average waveform (mean 6.48 mL/s, Figure 2.3a) [27]. Both use ensemble averaging based on aligning key feature points, which is important in preserving high frequency components in the waveform. For the purpose of the present study the two waveforms were normalized to have the same mean flow rate (6 mL/s).

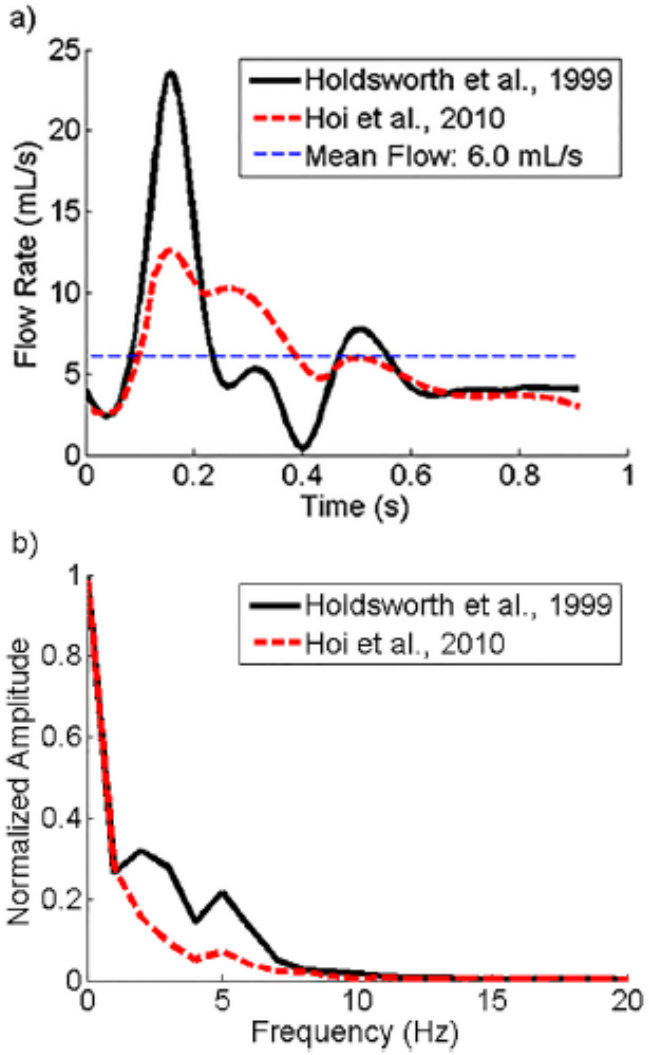

Figure 2.3: (a) The flow-rate waveforms representing "young" adults (Holdsworth et al., 1999) and "old" adults (Hoi et al., 2010) used in this study as described in the text and (b) corresponding frequency content for each.

2.2.2 Theoretical Model

A lumped parameter model was used specifically to (i) match the elements of the experimental setup and (ii) allow us to run scenarios that were beyond the range of parameters of the experimental setup. The model included the three basic elements of resistance (R), compliance (C) and inertance (L), arranged as shown in Figure 2.2c. The impedances of the ICA and ECA branches, respectively, and the total impedance of the system, are then given by:

$$Z_{ica}(\omega) = R_{ica} + i\omega L_{ica} + \frac{R_{id}}{R_{id}(i\omega C_{id} + i\omega C_{ica}) + 1} \quad 2.1$$

$$Z_{eca}(\omega) = R_{eca} + i\omega L_{eca} + \frac{R_{ed}}{R_{ed}(i\omega C_{ed} + i\omega C_{eca}) + 1} \quad 2.2$$

$$Z_{total}(\omega) = \frac{Z_{ica} Z_{eca}}{Z_{ica} + Z_{eca}} \quad 2.3$$

The pressure waveform $p(t)$ measured at the CCA inlet of the in vitro flow loop was used as input pressure to the theoretical LP model to obtain the corresponding flow waveform $q(t)$ using fast Fourier transform (FFT) and the harmonic relation:

$$q_i = \frac{p_i}{Z_i} \quad 2.4$$

where 'i' is the harmonic index and Z is impedance of the flow loop being tested. The theoretical flow waveform was then compared with a measured flow waveform and values of the parameters R, L, C were adjusted iteratively to achieve the best agreement (maximum $\mathcal{R}^2$ – goodness of fit) between the two. The final values of R, L, C were then deemed to be the parameter values characterizing the flow loop being tested. All analysis was done using MATLAB.

2.2.3 Experimental Protocol

Reduced flow loops that did not include the phantom (Figure 2.2b), together with a corresponding LP model (Eqs. 2.5-2.6), were used in order to establish the values of downstream elements of the experimental setup. There were four such reduced loops, representing either downstream of the ICA or downstream of the ECA, and in each case one without the CT section (to determine R_{id} and R_{ed} with C = 0, assuming all other tubing rigid) and one with the CT inserted (C ≠ 0). Pressure and flow waveforms were measured in each loop and a corresponding flow waveform was generated using the LP model for that loop with the following impedances:

$$Z_{id}(\omega) = i\omega L_{id} + \frac{R_{id}}{i\omega R_{id} C_{id} + 1} \tag{5}$$

$$Z_{ed}(\omega) = i\omega L_{ed} + \frac{R_{ed}}{i\omega R_{ed} C_{ed} + 1} \tag{6}$$

The values of $R_{id}, C_{id}, R_{ed},$ and C_{ed} were then held fixed for all subsequent experiments that included the phantom. The values of L_{id} and L_{ed} were not retained in subsequent experiments because they represent inertial effects specific to the reduced flow loops only and thus inertial effects in the full flow loops were expected to be different.

With the R and C values of downstream elements established, pressure and flow measurements were then made in the full flow loop configuration (Figure 2.2a) at the three locations indicated for each of the five phantoms: rigid with no stenosis, 30%, 50%, 70% stenosis, and compliant with 50% stenosis. Additionally, measurements made at the outlets of the phantom ICA and ECA were input directly to their respective reduced LP models described in Eqs. 2.5-2.6 to verify the derived downstream impedance values.

2.2.4 Statistical Analysis

A one-way ANOVA with Tukey post-hoc analysis was performed on all parameter values derived using the LP model. An $\mathcal{R}^2$ metric was used to quantify how well the experimental and modeled flow waveforms matched. The range of parameter values that maximized the $\mathcal{R}^2$ of the waveform fit to within ±0.0001 was used to obtain a mean and uncertainty for each parameter value. A one-way ANOVA with Tukey post-hoc analysis was also performed on the mean flow rate values averaged over 30 cardiac cycles and obtained on five different days for each of the five different phantoms and for both the ICA and CCA flow to establish uncertainty values. All statistical analysis done via Prism.

2.3 Results

Figure 2.4a shows the modelled and measured flow-rate waveforms for a reduced flow loop containing only the downstream resistance (i.e. resistive elements in Figure 2.2b) for the ICA, without the CT component. The downstream resistance (R_{id}), as listed in Table

2.1, was determined by setting $C_{id} = 0$ in Eq. 5. The same process was repeated with the ECA resistive loop to determine R_{ed}. Figure 2.4b shows the modelled and measured flow rate waveforms for a reduced flow loop to be attached downstream from the ICA containing both resistive and compliant components (with CT). Eq. 2.5 was used to determine the impedance by using the previously determined R_{id} to iteratively derive C_{id}. The same process was repeated for the other reduced flow loop to determine C_{ed}. Any additional resistance due to the larger diameter CT was considered negligible (<1%) compared to that of the flow resistor (FR). Identical segments of compliant tubing were used for the ICA and ECA flow loops, and the average compliance is given in Table 2.1. Figure 2.4c shows the measured and modelled waveforms at the outlets of the phantom ECA and ICA for the rigid 50% stenosed phantom. Already determined downstream parameter values were used to calculate the impedance.

Table 2.1: LP model parameters obtained for a family of four carotid geometries and two phantom compliances as determined by matching the theoretical and experimentally measured flow-rate waveforms (mean flow-rates measured in the ICA and CCA are listed).

	Rigid Normal	**Rigid 30%**	**Rigid 50%**	**Rigid 70%**	**Compliant 50%**
$\mathbf{R_{ed}}$	38.5 ± 0.5	38.5 ± 0.5	38.5 ± 0.5	38.5 ± 0.5	38.5 ± 0.5
$\mathbf{C_{ed}}$	2.40 ± 0.05	2.40 ± 0.05	2.40 ± 0.05	2.40 ± 0.05	2.40 ± 0.05
$\mathbf{R_{id}}$	24.2 ± 0.4	24.2 ± 0.4	24.2 ± 0.4	24.2 ± 0.4	24.2 ± 0.4
$\mathbf{C_{id}}$	2.40 ± 0.05	2.40 ± 0.05	2.40 ± 0.05	2.40 ± 0.05	2.40 ± 0.05
$\mathbf{R_{ica}}$	0.44 ± 0.06	0.92 ± 0.06 *	1.30 ± 0.14 **	2.56 ± 0.14 ***	1.30 ± 0.14 **
$\mathbf{C_{ica}}$	0.35 ± 0.07 †††	0.41 ± 0.02 †††	0.58 ± 0.11 †††	0.59 ± 0.01 †††	1.86 ± 0.08
$\mathbf{L_{ica}}$	0.29 ± 0.01	0.30 ± 0.01	0.30 ± 0.01	0.32 ± 0.01	0.30 ± 0.01
$\mathbf{R_{eca}}$	0.84 ± 0.05	0.84 ± 0.05	0.84 ± 0.05	0.84 ± 0.05	0.84 ± 0.05
$\mathbf{C_{eca}}$	0.35 ± 0.07 †††	0.41 ± 0.02 †††	0.58 ± 0.11 †††	0.59 ± 0.01 †††	1.86 ± 0.08
$\mathbf{L_{eca}}$	0.29 ± 0.01	0.30 ± 0.01	0.30 ± 0.01	0.32 ± 0.01	0.30 ± 0.01
Mean ICA Flow	3.74 ± 0.10 †	3.72 ± 0.07 †	3.70 ± 0.09 ††	3.56 ± 0.08 $^{** \dagger\dagger\dagger}$	3.88 ± 0.12
Mean CCA Flow	6.00 ± 0.07	5.98 ± 0.05	6.08 ± 0.09	5.94 ± 0.12	6.08 ± 0.08

* $p<0.05$, ** $p<0.01$, *** $p<0.001$ compared to rigid normal.
† $p<0.05$, †† $p<0.01$, ††† $p<0.001$ compared to compliant 50%.
Units: [L: mmHg/(mL/s^2)] [R: mmHg/(mL/s)] [C: 10^{-3}mL/mmHg] [Flow: mL/s]

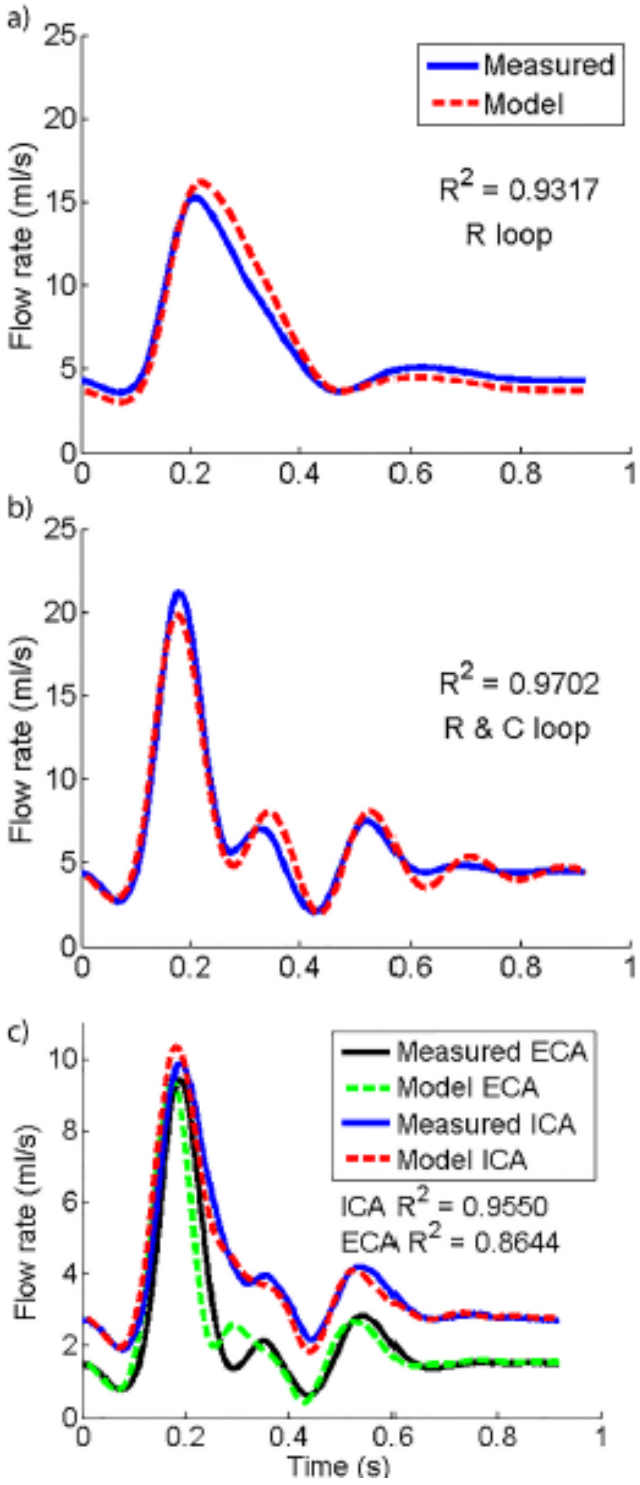

Figure 2.4: Measured and modelled waveforms obtained in the (a) downstream resistance only loop, (b) downstream resistance and compliance loop and (c) at the ECA and ICA outlets for a rigid carotid phantom with 50% stenosis.

Figure 2.5 shows the measured and modelled waveforms at the CCA inlet for the four rigid phantoms with no stenosis, 30%, 50%, and 70% stenosis. The full LP model was used, with all downstream R and C values as previously determined. The remaining parameters were iteratively derived where the experimental and theoretical flow waveforms were well matched $\mathcal{R}^2 > 0.97$ in all cases. The results (Table 2.1) showed that only in the severe 70%-stenosis case the resistance R_{ica} was significantly affected ($p<0.01$), increasing to 2.6 ± 0.1 mmHg/(mL/s), which is approximately an order of magnitude smaller than the downstream ICA and ECA resistance (Table 1).

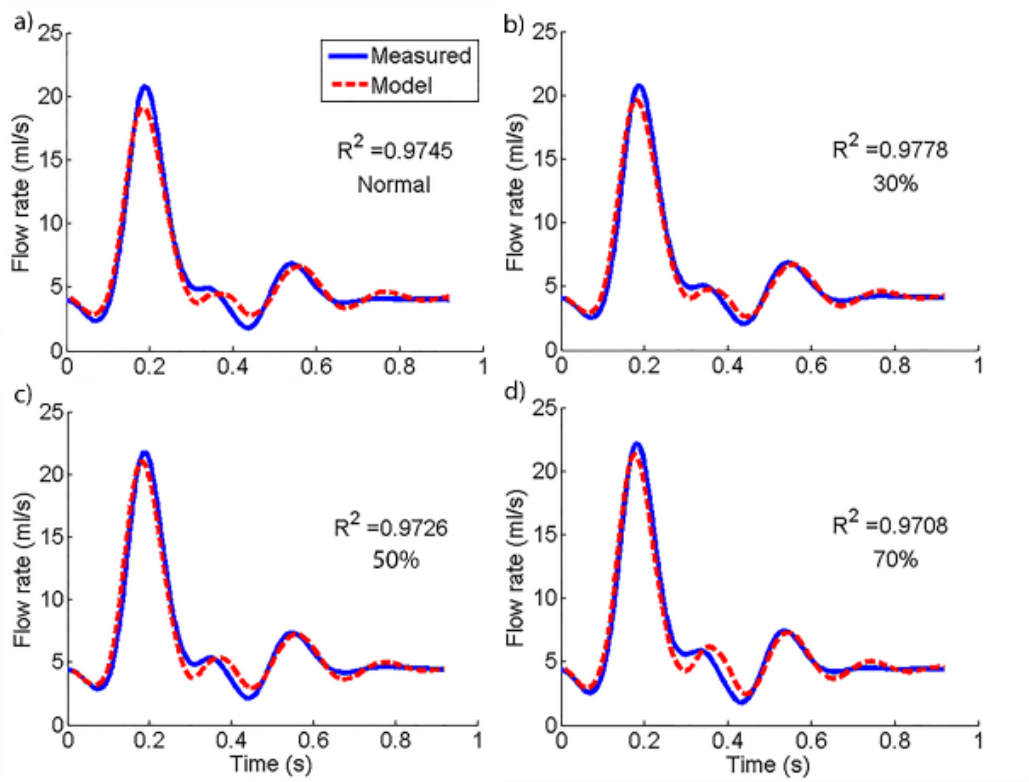

Figure 2.5: Measured and calculated flow waveforms at the CCA inlet of the rigid phantoms with (a) no stenosis, (b) 30%, (c) 50% and (d) 70% stenosis.

Figure 2.6 shows the modulus and phase of impedance for the first 12 harmonics measured and modelled at the CCA inlet of the compliant 50% stenosed phantom. Results for the "young" and "old" waveform are compared. Identical R, L, C parameters were used for the two waveforms to obtain a derived impedance (model). Agreement between the modelled and measured impedance plots for the two cases demonstrates that

the input waveform has little to no effect on the derived impedance. The matching of the waveforms also demonstrates that the derived impedance of the in vitro flow loop provided an accurate representation of the system.

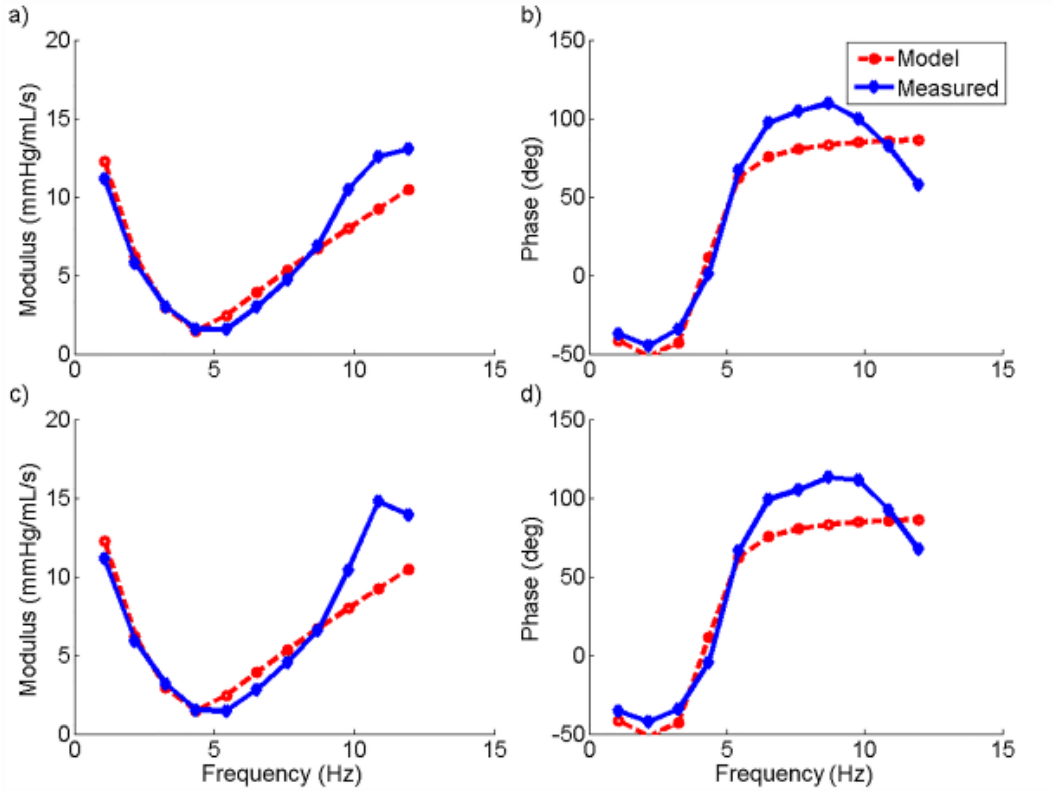

Figure 2.6: Measured and derived modulus and phase of impedance for the first 12 harmonics at the CCA inlet of the compliant 50% stenosed phantom. Results for the "young" and "old" waveform are shown in the top (a,b) and bottom (c,d) panels respectively.

Figure 2.7 shows the corresponding R_{ica} (resistance), mean ICA flow rates and CCA pressure waveforms with increasing stenosis. The increase in R_{ica} was significantly higher with increasing stenosis level, and this resulted in a correspondingly significant decrease (4.8%, $p<0.01$) in mean ICA flow rate at a 70% stenosis severity shown in Figure 2.7b. The increasing ICA resistance diverts more flow to the ECA branch where the resistance remains fixed. Figure 2.8a and 2.8b show the effect of reduced carotid artery compliance (C_{ica}, C_{eca}) on mean ICA flow rate. Specifically, the mean ICA flow

rate decreased significantly (4.6%, $p<0.01$) when the carotid compliance decreased from 0.00186 to 0.00058 mL/mmHg ($p<0.001$), a change of approximately a factor of 3, comparable with the three-fold increase in elastic modulus observed in vivo between the ages of 25 and 75 (Lanne et al., 1994). The relative importance of vessel compliance is further demonstrated by the higher ICA flow observed in a compliant 50%-stenosed phantom compared to a rigid normal (stenosis free) phantom.

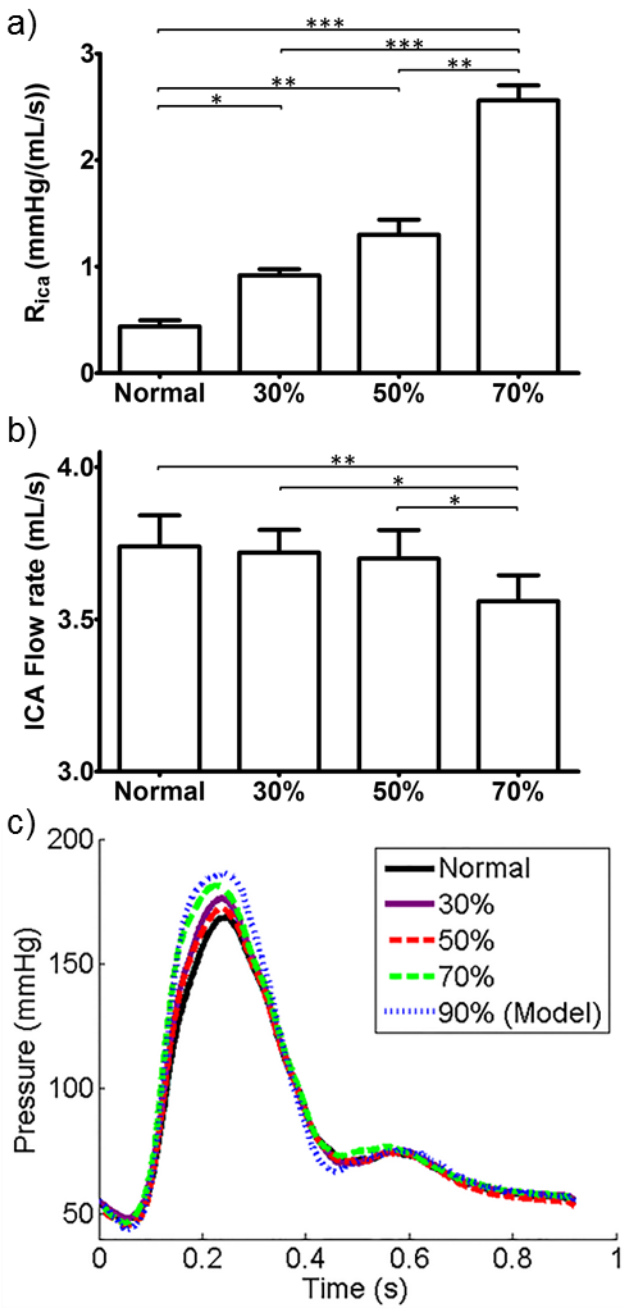

Figure 2.7: Effects of obstructive disease based on four different rigid phantoms of increasing stenosis. (a) Resistance of the ICA branch (R_{ica}) with increasing stenosis (significantly higher compared to normal - *p<0.05, **p<0.01, ***p<0.001) and (b) mean flow-rate through the ICA (significant for 70% stenosis compared to normal, p<0.01). (c) The measured CCA pressure waveforms are shown for the four rigid phantoms with increasing stenosis, as well as the extended case of 90% stenosis.

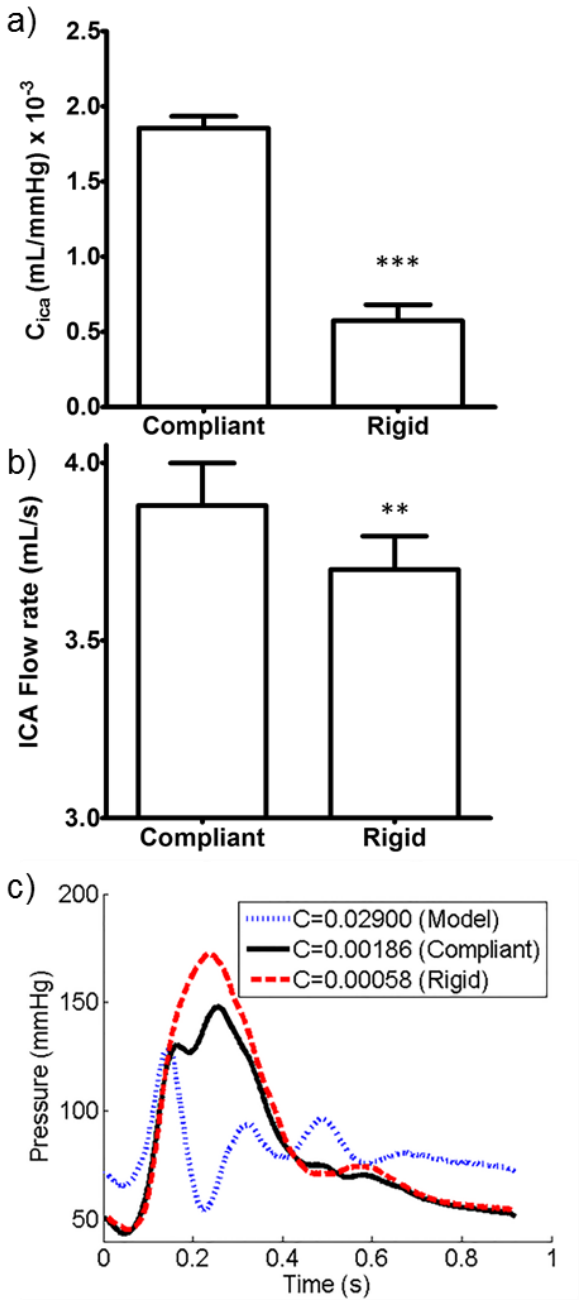

Figure 2.8: Effects of sclerotic disease based on comparing a pair of compliant and rigid phantoms, both with 50% ICA stenosis. (a) Compliance of the ICA (C_{ica}) as determined for the two phantoms, showing a significant difference ($p<0.001$). (b) Corresponding difference in mean ICA flow rate ($p<0.01$). (c) Experimentally measured pressure waveforms in the rigid and compliant 50% stenosed phantoms are shown for comparison with the modelled pressure waveform in the extended case with physiological compliance.

The LP model was used to extend the study to two specific cases below, for which phantoms were not available. In the first case, the resistance R_{ica} was increased to 3.31 mmHg/(mL/s), to represent a stenosis of 90% as determined by Kaluzynski et al. (2003) [21]. The measured CCA flow-rate waveform from the rigid 70%-stenosed phantom was used as an estimate to derive the pressure waveform for the more severely (90%) stenosed case. This is based on the assumption that the volumetric-displacement pump ensures a fixed CCA inlet flow as programmed and further demonstrated by the fact that no statistical changes are observed in mean CCA flow rates (Table 2.1). Figure 2.7c shows the measured pressure waveforms for the rigid normal, 30%, 50% and 70% stenosed phantoms as well as the modelled pressure waveform for the extended 90% stenosis case. The systolic pressures increase slightly with increasing stenosis.

In the second case, a more physiologically realistic compliance than available in the phantoms was tested to study the resulting changes in the pressure waveform. The CCA flow-rate waveform measured for the compliant phantom was used as an approximation for the extended case. Figure 2.8c shows measured pressure waveforms for the rigid and compliant 50% stenosed phantoms as well as a modelled pressure waveform reflecting an increase in the carotid compliance (C_{ica}, C_{eca}) to 0.0290 mL/mmHg based on Kaluzynski et al. (2003) [21] and representative of physiological compliance. The resulting pressure waveform displays a much lower systolic pressure, which is in the normotensive range of approximately 120 mmHg.

Figure 2.9 explores the effects of changing the values of downstream parameters (different values reported in the literature [21, 29-30]) ($R_{id}, R_{ed}, C_{id}, C_{ed}$) in the flow loop containing the rigid 50% stenosed phantom. The measured pressure waveform and the resulting modelled flow-rate waveform with already derived downstream resistance R_0 and compliance C_0 are used as the baseline. Using the baseline pressure waveform, values of the downstream resistance (R_{id}, R_{ed}) are changed drastically in both directions from the baseline value (R_0) and the resulting CCA flow-rate waveforms are shown in Figure 2.9a. While in Figure 2.9c, C_{id} and C_{ed} are changed from the baseline compliance (C_0) and again resulting CCA flow-rate waveforms are shown. The results are tabulated in Figure 2.9b and 2.9d for corresponding changes in the downstream parameters

alongside the mean CCA flow rates (cycle averaged from the corresponding waveforms shown in panels a and c) and the extrapolated mean ICA flow rates (based on the ratio of 3.70 mL/s to 6.08 mL/s as determined experimentally – Table 1). Figure 2.9c also shows that a flow-rate waveform shape similar to that seen in 'old' adults could be generated from an input pressure waveform corresponding to the 'young' adult flow-rate waveform by reducing the compliance by a factor of 2. The general shape of the two flow-rate waveforms can be seen in Figure 2.3a. Likewise, the converse could be achieved by using a pressure waveform corresponding to the 'old' adult waveform and increasing the compliance by a factor of 2 to generate the 'young' waveform (not shown).

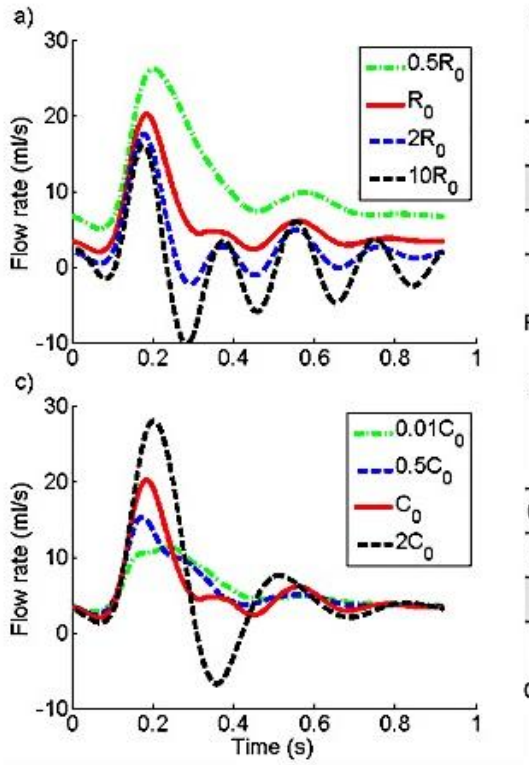

b)

	R_{id}	R_{ed}	Mean CCA Flow	Mean ICA Flow
$0.5R_0$	12.1	19.3	10.8	6.59
R_0	24.2	38.5	5.61	3.42
$2R_0$	48.4	77.0	2.86	1.74
$10R_0$	242.0	385.0	0.58	0.35

R: [mmHg/(mL/s)], Flow: [mL/s]

d)

	C_{id}	C_{ed}	Mean CCA Flow	Mean ICA Flow
$0.01C_0$	0.024	0.024	5.61	3.42
$0.5C_0$	1.2	1.2	5.61	3.42
C_0	2.4	2.4	5.61	3.42
$2C_0$	4.8	4.8	5.61	3.42

C: [10^{-3}mL/mmHg], Flow: [mL/s]

Figure 2.9: CCA flow-rate waveforms (a,c) and mean CCA and ICA flow rates (b,d) are shown with changing downstream parameters in the flow loop containing the rigid 50% stenosed phantom. Model values of the downstream resistance (a,b) and compliance (c,d) are changed drastically in both directions relative to the baseline values (R_0, C_0) derived for the experimental setup.

2.4 Discussion and Conclusions

A combination of a lumped parameter model and an experimental in vitro carotid artery flow system was used to study how local carotid artery pathologies that cause obstruction or stiffening may impact blood supply to the brain via the ICA. The theoretical model was verified through the use of different experimental configurations, phantoms, and waveforms. This was important because it allowed us to extend the scope of the study beyond the range of phantoms that were available in the experiment. More importantly, it allowed us also to explore a range of parameters (representing vasculature downstream of the internal and external carotid arteries) for which only limited physiological data exists. We are able to separately study the roles of resistance and compliance.

Local changes in compliance of the carotid arteries were found to have a significant effect on mean flow-rate through the ICA (i.e. flow fraction) and on the pressure waveforms measured at the inlet of the CCA, thus affecting blood supply to the brain (Figure 2.8). This is particularly important because sclerotic disease and aging have a severe impact on vessel compliance. Age alone has been shown to increase the elastic modulus (thus reduce the elasticity and compliance) by approximately a factor of three between the ages of 25 and 75 [15, 31]. The change in pressure waveform that we observed is consistent with the difference between the "young" and "old" waveforms reported by Holdsworth et al. (1999) [28] and Hoi et al. (2010) [27], respectively which represent age groups of 28 ± 3 and 68 ± 8 years. Reduced vascular compliance has also been associated with injury or cardiovascular disease [32]. Hypertension, atherosclerosis and congestive heart failure have been reported to increase the value of the elastic modulus by approximately a factor of 2 [33-35].

While the changes found with 'sclerotic disease' in our study are statistically significant (~5% reduction in mean ICA flow rate), they are not necessarily significant in the physiological system. Often the contralateral side compensates for any reduction in blood flow. This could be a reasonable extrapolation for a stenosed carotid artery; however, sclerotic disease is likely to have a more systemic effect whereby all arteries have reduced compliance. Contingent on how this manifests in vivo, it could potentially lead

to an overall reduction in blood flow reaching the brain (Figure 2.8) and will also alter the waveform shape as shown in Figure 2.8-2.9.

Effects of increased local stenosis in the internal carotid artery on mean flow-rate in the ICA and pressure waveform at the inlet of the CCA, and hence on blood flow to the brain, were found to be minimal up to a threshold of 70% stenosis (Figure 2.7). This is consistent with the reality that the resistance of the carotid artery is relatively small compared with the overall resistance of downstream vasculature, and therefore a small change in the resistance of the carotid artery would not lead to significant effects on flow rate. These findings are consistent with reports in the literature that ICA flow-rates appear only to be affected by "severe stenosis"; approximately ≥60% [36], above 80% stenosis [37] or "multiple moderate stenosis" [38]. It has been generally acknowledged that flow reduction due to carotid stenosis itself may not be the primary cause of ischemic stroke [39-40]. Our results are consistent with this view in that a small but statistically significant reduction in ICA flow was observed only above 70% stenosis.

Comparison to quoted literature values (Table 2.2) suggests that our downstream resistance is within a factor of 2 of other model based estimations but downstream compliance is up to a factor of 10 lower [21, 29-30]. However, literature surrounding these values is both incomplete and inconsistent. For this reason, a range of different downstream resistance and compliance values were tested to study the effects of changes in downstream parameters. Changes in downstream resistance resulted in changes to the mean CCA flow rate and thus ICA flow rate (Figure 2.9a-b). Changes in downstream compliance resulted in dramatic changes to waveform shape and pulsatility, while no changes in mean CCA (and thus ICA) flow rates were observed (Figure 2.9c-d). The significance of compliance is further demonstrated as an 'old' adult waveform shape was generated from the 'young' adult waveform by reducing the compliance by a factor of 2. This suggests that the 'old' adult waveform is essentially a low compliance version of the 'young' adult waveform as elastic modulus often increases by a factor of 3 between the ages of 25 to 75. The ability of the model to replicate this with a change in downstream compliance is one of its strengths. Further studies will attempt to demonstrate this experimentally.

Both Figure 2.8 and Figure 2.9c-d explore the effects of changes in compliance. In Figure 2.8, increased carotid phantom compliance resulted in increased mean ICA flow rates. In this case, a fixed CCA flow-rate waveform was used but mean ICA flow-rate increased due to changes in the ICA to ECA flow division for a portion of the cardiac cycle (flow division for the rigid phantom can be seen in Figure 2.4c and Appendix D). We postulate that the increased compliance caused a decrease in resistance in the ICA branch (stenosis) and thus resulted in an increased mean ICA flow rate seen in Figure 2.8b. In Figure 2.9c-d, changes in downstream compliance results in no changes in mean ICA flow rates. In this case, a fixed CCA pressure waveform is used as an input and CCA flow rate waveforms are allowed to vary with changing compliance. Theoretically, compliance only affects the oscillatory portion of the waveforms and the mean flow should not be affected hence mean CCA flow rates are maintained. As well, since these compliant components are placed downstream of the bifurcation and both altered symmetrically, the flow division between the ICA and ECA is not affected.

Table 2.2: Quoted downstream parameter values in the literature.

Reference	Quoted Downstream Parameter Values
Alastruey et al., (2014) Generated numerically in models of human compliant vessels by solving non-linear 1D equations of blood flow in 55 larger systemic artery segments.	R_{id} = 14.10 mmHg/(mL/s) R_{ed} = 78.16 mmHg/(mL/s) C_{id} = 0.0252 mL/mmHg C_{ed} = 0.0231 mL/mmHg Mean flow: ICA = 5.8 mL/s Mean flow: ECA = 0.7 mL/s
Kaluzynski et al., (2003) Downstream resistance as used experimentally in the in vitro flow loop and derived using a 10 element transmission line model.	R_{id} = 12.75 mmHg/(mL/s) R_{ed} = 28.5 mmHg/(mL/s) C_{id} = 0.014 mL/mmHg C_{ed} = 0.016 mL/mmHg
Toorop et al., (1987) Peripheral Overall peripheral resistance derived using 3-element LP model (not for a specific vascular bed).	Peripheral Resistance – 26.55 mmHg/(mL/s) Aortic Compliance – 0.037 mL/mmHg

Limitations: A major difficulty in any theoretical or experimental study of the effects of carotid artery disease on blood flow to the brain is the lack of complete and accurate data

on the parameter values of vasculature downstream of the ICA and ECA, which includes the brain vasculature. Our combination of theoretical and experimental methodology, using one to validate the other, allowed us to overcome this difficulty somewhat by exploring a very wide range of possible downstream values. Ultimately, however, data on downstream vasculature are essential for a more accurate assessment of the effects of carotid artery disease on blood flow to the brain. Also, the LP model does not account for the effects of wave reflections, although some of these effects may be imbedded within the inductance parameter 'L'. This could be responsible for the slight mismatch seen between some modelled and measured flow-rate waveforms. Phantom compliance was well below physiological levels, thus the LP model was used to extend the study to include physiological compliance. Wada et al. (1991) [38] demonstrated that the presence of a stenosis reduced overall CCA flow rates which would be in addition to decreased ICA flow fraction shown here.

2.5 References

[1] Sobieszczyk, P. and J. Beckman, *Carotid artery disease.* Circulation, 2006. **114**(7): p. e244-7.

[2] Barnett, H.J., et al., *Benefit of carotid endarterectomy in patients with symptomatic moderate or severe stenosis. North American Symptomatic Carotid Endarterectomy Trial Collaborators.* N Engl J Med, 1998. **339**(20): p. 1415-25.

[3] Ferguson, G.G., et al., *The North American Symptomatic Carotid Endarterectomy Trial : surgical results in 1415 patients.* Stroke, 1999. **30**(9): p. 1751-8.

[4] Domanski, M., et al., *Can we dramatically reduce the incidence of coronary heart disease?* Nat Rev Cardiol, 2011. **8**(12): p. 721-5.

[5] Gijsen, F.J., et al., *Strain distribution over plaques in human coronary arteries relates to shear stress.* Am J Physiol Heart Circ Physiol, 2008. **295**(4): p. H1608-14.

[6] Kefayati, S., et al., *In vitro shear stress measurements using particle image velocimetry in a family of carotid artery models: effect of stenosis severity, plaque eccentricity, and ulceration.* PLoS One, 2014. **9**(7): p. e98209.

[7] Leach, J.R., et al., *Carotid atheroma rupture observed in vivo and FSI-predicted stress distribution based on pre-rupture imaging.* Ann Biomed Eng, 2010. **38**(8): p. 2748-65.

[8] Malek, A.M., S.L. Alper, and S. Izumo, *Hemodynamic shear stress and its role in atherosclerosis.* JAMA, 1999. **282**(21): p. 2035-42.

[9] Sadat, U., et al., *Association between biomechanical structural stresses of atherosclerotic carotid plaques and subsequent ischaemic cerebrovascular events--a longitudinal in vivo magnetic resonance imaging-based finite element study.* Eur J Vasc Endovasc Surg, 2010. **40**(4): p. 485-91.

[10] Slager, C.J., et al., *The role of shear stress in the destabilization of vulnerable plaques and related therapeutic implications.* Nat Clin Pract Cardiovasc Med, 2005. **2**(9): p. 456-64.

[11] Steinman, D.A., et al., *Flow patterns at the stenosed carotid bifurcation: effect of concentric versus eccentric stenosis.* Ann Biomed Eng, 2000. **28**(4): p. 415-23.

[12] Teng, Z., et al., *3D critical plaque wall stress is a better predictor of carotid plaque rupture sites than flow shear stress: An in vivo MRI-based 3D FSI study.* J Biomech Eng, 2010. **132**(3): p. 031007.

[13] Vengrenyuk, Y., et al., *A hypothesis for vulnerable plaque rupture due to stress-induced debonding around cellular microcalcifications in thin fibrous caps.* Proc Natl Acad Sci U S A, 2006. **103**(40): p. 14678-83.

[14] Wentzel, J.J., et al., *Endothelial shear stress in the evolution of coronary atherosclerotic plaque and vascular remodelling: current understanding and remaining questions.* Cardiovasc Res, 2012. **96**(2): p. 234-43.

[15] Lanne, T., et al., *Differences in mechanical properties of the common carotid artery and abdominal aorta in healthy males.* J Vasc Surg, 1994. **20**(2): p. 218-25.

[16] Poepping, T.L., et al., *An in vitro system for Doppler ultrasound flow studies in the stenosed carotid artery bifurcation.* Ultrasound Med Biol, 2002. **28**(4): p. 495-506.

[17] Stergiopulos, N., J.J. Meister, and N. Westerhof, *Evaluation of methods for estimation of total arterial compliance.* Am J Physiol, 1995. **268**(4 Pt 2): p. H1540-8.

[18] Stergiopulos, N., B.E. Westerhof, and N. Westerhof, *Total arterial inertance as the fourth element of the windkessel model.* American Journal of Physiology-Heart and Circulatory Physiology, 1999. **276**(1): p. H81-H88.

[19] Westerhof, N., G. Elzinga, and P. Sipkema, *An artificial arterial system for pumping hearts.* Journal of Applied Physiology, 1971. **31**(5): p. 776-81.

[20] Zamir, M., *The Physics Of Coronary Blood Flow.* Biological and medical physics, biomedical engineering. 2005, New York: Springer. xvii, 408 p.

[21] Kaluzynski, K., et al., *Studies of Arterial Input Impedance in Models of Carotid Artery.* Journal of Mechanics in Medicine and Biology, 2003. **3**(1): p. 9-19.

[22] Kefayati, S. and T.L. Poepping, *Transitional flow analysis in the carotid artery bifurcation by proper orthogonal decomposition and particle image velocimetry.* Med Eng Phys, 2013. **35**(7): p. 898-909.

[23] Holdsworth, D.W., et al., *Computer-controlled positive displacement pump for physiological flow simulation.* Med Biol Eng Comput, 1991. **29**(6): p. 565-70.

[24] Yousif, M.Y., D.W. Holdsworth, and T.L. Poepping, *A blood-mimicking fluid for particle image velocimetry with silicone vascular models.* Experiments in Fluids, 2011. **50**(3): p. 769-774.

[25] Bartlett, E.S., et al., *Quantification of carotid stenosis on CT angiography.* AJNR Am J Neuroradiol, 2006. **27**(1): p. 13-9.

[26] Eliasziw, M., et al., *Further comments on the measurement of carotid stenosis from angiograms. North American Symptomatic Carotid Endarterectomy Trial (NASCET) Group.* Stroke, 1994. **25**(12): p. 2445-9.

[27] Hoi, Y., et al., *Characterization of volumetric flow rate waveforms at the carotid bifurcations of older adults.* Physiol Meas, 2010. **31**(3): p. 291-302.

[28] Holdsworth, D.W., et al., *Characterization of common carotid artery blood-flow waveforms in normal human subjects.* Physiol Meas, 1999. **20**(3): p. 219-40.

[29] Alastruey, J., A.A. Hunt, and P.D. Weinberg, *Novel wave intensity analysis of arterial pulse wave propagation accounting for peripheral reflections.* Int J Numer Method Biomed Eng, 2014. **30**(2): p. 249-79.

[30] Toorop, G.P., N. Westerhof, and G. Elzinga, *Beat-to-beat estimation of peripheral resistance and arterial compliance during pressure transients.* Am J Physiol, 1987. **252**(6 Pt 2): p. H1275-83.

[31] Hansen, F., et al., *Diameter and compliance in the human common carotid artery--variations with age and sex.* Ultrasound Med Biol, 1995. **21**(1): p. 1-9.

[32] Seals, D.R., *Habitual exercise and the age-associated decline in large artery compliance.* Exerc Sport Sci Rev, 2003. **31**(2): p. 68-72.

[33] Arcaro, G., et al., *Stiffness of the common carotid artery in treated hypertensive patients.* J Hypertens, 1991. **9**(10): p. 947-54.

[34] Labropoulos, N., et al., *Viscoelastic properties of normal and atherosclerotic carotid arteries.* Eur J Vasc Endovasc Surg, 2000. **19**(3): p. 221-5.

[35] Lage, S.G., et al., *Carotid arterial compliance in patients with congestive heart failure secondary to idiopathic dilated cardiomyopathy.* Am J Cardiol, 1994. **74**(7): p. 691-5.

[36] Levine, R.L., et al., *Comparison of magnetic resonance volume flow rates, angiography, and carotid Dopplers. Preliminary results.* Stroke, 1994. **25**(2): p. 413-7.

[37] Spencer, M.P. and J.M. Reid, *Quantitation of carotid stenosis with continuous-wave (C-W) Doppler ultrasound.* Stroke, 1979. **10**(3): p. 326-30.

[38] Wada, T., et al., *Correlation of common carotid flow volume measured by ultrasonic quantitative flowmeter with pathological findings.* Stroke, 1991. **22**(3): p. 319-23.

[39] Barnett, H.J., et al., *Causes and severity of ischemic stroke in patients with internal carotid artery stenosis.* JAMA, 2000. **283**(11): p. 1429-36.

Chapter 3

3 Conclusions and Future Directions

A lumped parameter model was successfully designed to match the existing in vitro flow loop mimicking vascular flow though the carotid artery bifurcation. The downstream model parameters were determined using four reduced loops (Figure 2.2b and Appendix C) - containing the resistive and compliant elements located downstream from the ICA and ECA. The remaining parameters were determined using simultaneous pressure and flow-rate measurements made at the inlet of the CCA of the full flow loop (Figure 2.2a). Two different waveforms ('young' and 'old') were also tested in the flow loop to study their impedance characteristics. The changes in mean flow-rate and waveform shape were studied.

3.1 Conclusions

There were four specific cases explored in this thesis:

1) As the stenosis of the rigid phantoms was increased, so was the resulting resistance parameter (R_{ica}) used to model it. This increase in resistance also resulted in a subsequent decrease in mean ICA flow-rate that was only statistically significant at a 70% stenosis level consistent with the literature [1-2]. Furthermore, increases in systolic pressure were observed for increasing stenosis levels in the CCA pressure waveforms while general waveform shape is maintained. The study was further extended by using the LP model to a severe (90%) stenosis case by increasing R_{ica}. The same trend was observed as a further increase in systolic pressure occurred.

2) Two phantoms with different compliances were studied (C_{ica}, C_{eca}). The difference in compliance was a factor of 3, similar to what is observed in vivo with aging [3] but the actual compliance of the phantoms was well below physiological compliance [4]. Mean ICA flow-rate was found to decrease with

decreasing compliance. We postulate that this is the result of a decrease in resistance in the stenosis region (not reflected in our parameter values) as higher mean ICA flow-rates are observed in the compliant 50% stenosed phantom than the rigid normal phantom. A significant change was also observed in the shape of the CCA pressure waveforms and the resulting systolic pressure. The study was further extended using the LP model to include physiological compliance where further drastic changes were observed in the pressure waveform and systolic pressures dropped to normotensive levels.

3) The LP model was used to extend the study to examine the effects of changes in downstream resistance (R_{id}, R_{ed}). Using the pre-determined values of downstream resistance as a baseline (R_0), CCA flow-rate waveforms for the rigid 50% stenosed phantom are plotted. The changes in R_0 minimally alter the general waveform shape but mean CCA (and ICA) flow rates are significantly altered where mean ICA flow-rates were extrapolated from the experimental ICA to CCA ratio provided in Table 2.1.

4) The LP model was used to extend the study to examine the effects of changes in downstream compliance (C_{id}, C_{ed}). Pre-determined values of downstream compliance were used as the baseline (C_0) to plot CCA flow-rate waveforms for the rigid 50% stenosed phantom. The changes in C_0 do not result in any changes in mean CCA (and thus ICA) flow-rates (although this might not be case experimentally depending on how these changes would manifest). The waveform shape is significantly altered with changes in compliance as seen previously with changes in phantom compliance. One of the most interesting results here is that using the ‘young’ [5] waveform, a waveform similar to the ‘old’ [6] waveform can be generated by a decrease in compliance and vice versa.

While changes in stenosis severity and thus resistance have previously been studied, compliance of both the carotid and downstream vasculature has been neglected. Our results for changes in carotid phantom compliance show that in terms of a reduction in mean ICA flow-rate, how compliance manifests is as significant as a severe stenosis.

Some limitations of our study included the limited data available for downstream vasculature [4, 7-9], and the lack of a phantom with physiological compliance.

3.2 Future Directions

While the degree of stenosis severity is the main indicator used in the clinic to classify at risk patients, it is well known that this is not the only risk factor. In fact, the geometry of the plaque plays a major role in thrombosis [10, 11-14]. Ulcerated plaques for example are more like to rupture and embolize [11-14]. The American Heart Association recommends surgical removal of plaques when stenosis severity is 70% or greater and 50% or greater if the plaque contains an ulceration [15]. Eccentricity of the plaque is another risk factor [10]. This study used only eccentrically stenosed phantoms. Future work will utilize existing phantoms with concentrically developed plaques and ulcerated plaques. The concentrically stenosed phantoms are available for the same stenosis levels as the eccentrically stenosed phantoms. The phantoms with ulcerated plaques contain ulcerations with different sizes. The impact of these subtle changes in the stenosis geometry on lumped parameters and waveform shape will be studied. It is hypothesized that ulcerated plaques will lead to an increase in both resistance and inductance while concentrically stenosed plaques could decrease them.

The phantoms used in this study are also utilized in the PIV system in the laboratory and for this reason, certain manufacturing limitations exist. For example: the phantom needs to be optically transparent and refractive index matched to our previous phantoms and blood mimicking fluid. The current thin-walled phantom that exists in our lab is manufactured from a PDMS (Sylgard 184) solution that has a compliance that is almost a magnitude lower than what is seen in vivo [4]. The laboratory is in the process of exploring different PDMS solutions (Sylgard 527 has shown some promise in other studies [16]) that are refractive index matched to build a phantom with (or closer to) physiological compliance. This phantom will serve to validate the predictions made in this study regarding the resulting waveform shape. The impact of physiological compliance on other parameters will also be studied.

One of the main results obtained in our study was the effects of changing downstream parameters. Changing downstream resistance resulted in changes to mean CCA flow-rates and changing downstream compliance resulted in changes to waveform shape. These results were all generated theoretically using the LP model. Further studies will attempt to demonstrate these effects experimentally. Changing both downstream compliance and resistance in the experimental setup is easier than attempting to change the phantom as none of the PIV restrictions apply here. Thus, downstream resistance can be altered by changing the length (or diameter) of the flow resistors and downstream compliance can be altered by changing the length of the compliant tubes or the stiffness of the tubes used. Preliminary results obtained from decreases in downstream compliance have managed to experimentally generate the 'old' waveform shape when the 'young' waveform is programmed to the pump.

Finally, the study of aneurysms is one of the emerging fields in vascular flow [17]. When an aneurysm bursts, a hemorrhagic stroke results. Hemorrhagic strokes make about 15% of all strokes but are more likely to result in death with a 40% mortality rate [18]. An existing aneurysm phantom in the lab will be used and a new in vitro flow loop will be constructed to simulate flow through the brain vasculature. Future studies will design a new LP model to match this flow loop. This LP model will be used to study the global characteristics of the system and changes in waveforms resulting from the aneurysm.

3.3 References

[1] Levine, R.L., et al., *Comparison of magnetic resonance volume flow rates, angiography, and carotid Dopplers. Preliminary results.* Stroke, 1994. **25**(2): p. 413-7.

[2] Spencer, M.P. and J.M. Reid, *Quantitation of carotid stenosis with continuous-wave (C-W) Doppler ultrasound.* Stroke, 1979. **10**(3): p. 326-30.

[3] Lanne, T., et al., *Differences in mechanical properties of the common carotid artery and abdominal aorta in healthy males.* J Vasc Surg, 1994. **20**(2): p. 218-25.

[4] Kaluzynski, K., et al., *Studies of Arterial Input Impedance in Models of Carotid Artery.* Journal of Mechanics in Medicine and Biology, 2003. **3**(1): p. 9-19.

[5] Holdsworth, D.W., et al., *Characterization of common carotid artery blood-flow waveforms in normal human subjects.* Physiol Meas, 1999. **20**(3): p. 219-40.

[6] Hoi, Y., et al., *Characterization of volumetric flow rate waveforms at the carotid bifurcations of older adults.* Physiol Meas, 2010. **31**(3): p. 291-302.

[7] Alastruey, J., A.A. Hunt, and P.D. Weinberg, *Novel wave intensity analysis of arterial pulse wave propagation accounting for peripheral reflections.* Int J Numer Method Biomed Eng, 2014. **30**(2): p. 249-79.

[8] Toorop, G.P., N. Westerhof, and G. Elzinga, *Beat-to-beat estimation of peripheral resistance and arterial compliance during pressure transients.* Am J Physiol, 1987. **252**(6 Pt 2): p. H1275-83.

[9] Nichols, W.W., M.F. O'Rourke, and C. Vlachopoulos, *McDonald's Blood Flow in Arteries: theoretic, experimental, and clinical principles*. 6th ed. 2011, London: Hodder Arnold. xiv,755 p.

[10] Ohara, T., et al., *Eccentric stenosis of the carotid artery associated with ipsilateral cerebrovascular events.* AJNR Am J Neuroradiol, 2008. **29**(6): p. 1200-3.

[11] Tousoulis, D., et al., *Angiographic characteristics of infarct-related and non-infarct-related stenoses in patients in whom stable angina progressed to acute myocardial infarction.* Am Heart J, 1998. **136**(3): p. 382-8.

[12] Young, D.F. and F.Y. Tsai, *Flow characteristics in models of arterial stenoses. I. Steady flow.* J Biomech, 1973. **6**(4): p. 395-410.

[13] Tang, D., et al., *Effect of stenosis asymmetry on blood flow and artery compression: a three-dimensional fluid-structure interaction model.* Ann Biomed Eng, 2003. **31**(10): p. 1182-93.

[14] Long, Q., et al., *Numerical investigation of physiologically realistic pulsatile flow through arterial stenosis.* J Biomech, 2001. **34**(10): p. 1229-42.

[15] Moore, W.S., et al., *Guidelines for carotid endarterectomy. A multidisciplinary consensus statement from the Ad Hoc Committee, American Heart Association.* Circulation, 1995. **91**(2): p. 566-79.

[16] Palchesko, R.N., et al., *Development of polydimethylsiloxane substrates with tunable elastic modulus to study cell mechanobiology in muscle and nerve.* PLoS One, 2012. **7**(12): p. e51499.

[17] Khan, M.O., K. Valen-Sendstad, and D.A. Steinman, *Narrowing the Expertise Gap for Predicting Intracranial Aneurysm Hemodynamics: Impact of Solver Numerics versus Mesh and Time-Step Resolution.* AJNR Am J Neuroradiol, 2015. **36**(7): p. 1310-6.

[18] WebMD - Stroke Health Center. *Understanding Stroke -- The Basics*. 2015 [cited 2015; Available from: http://www.webmd.com/stroke/guide/understanding-stroke-basics.

Appendix A

Expansion of Methods

Figure A.1 shows the chain of events that result in a theoretical flow-rate waveform starting from a measured input pressure waveform.

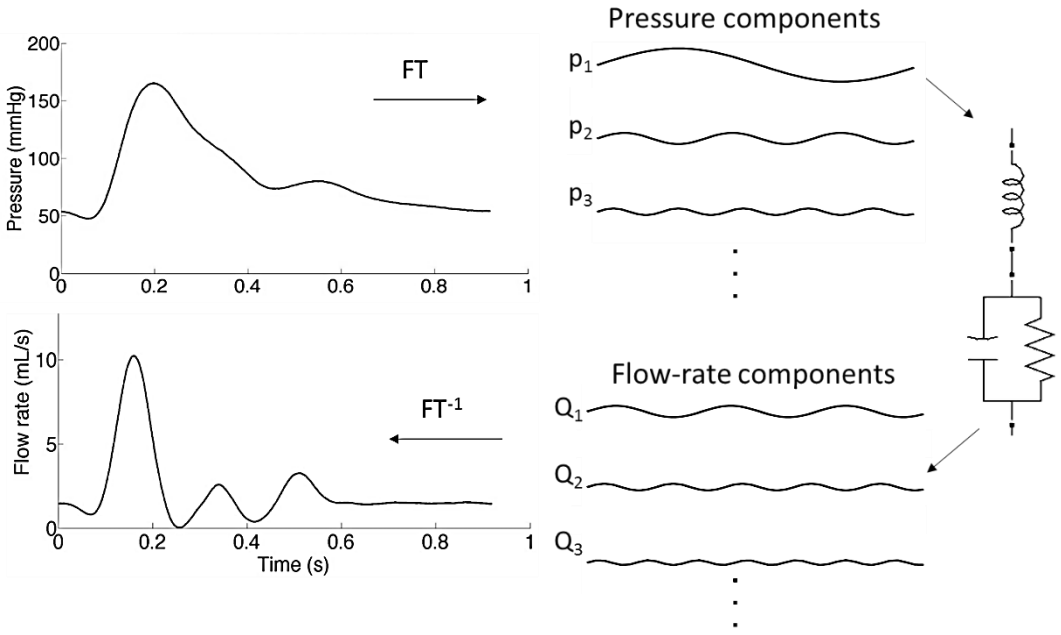

Figure A.1: A Fourier transform of the measured pressure waveform results in pressure frequency components that are divided by the impedance calculated from the LP model to generate flow-rate frequency components that are inversely transformed to obtain a theoretical flow-rate waveform. This theoretical waveform is matched to the experimentally measured waveform by iteratively varying the impedance parameters. For measurements made the inlet of the CCA in the full flow loop, the LP model shown in Figure 2.2c is used.

Figure A.2 shows the various Fourier transform methods used initially and verified against each other. After verification, the built-in MATLAB functions were adopted for simplicity.

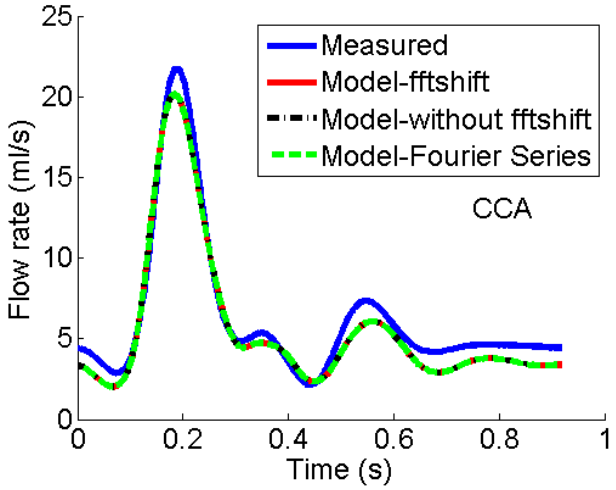

Figure A.2: Measured and modelled and waveforms are shown for the rigid 50% stenosed phantom at the inlet of the CCA. The modelled waveforms are shown using three different Fourier transform methods: with the built-in FFT and FFTshift functions, using the built-in FFT function but own FFTshift code and finally using own Fourier series code.

Figure A.3 shows 30 individual cardiac cycles that are averaged to give a typical waveform used in this study. As can be seen, one of the advantages of a physical system is that there is very little variability in the 30 cycles. The uncertainty of the average waveform is within marker size.

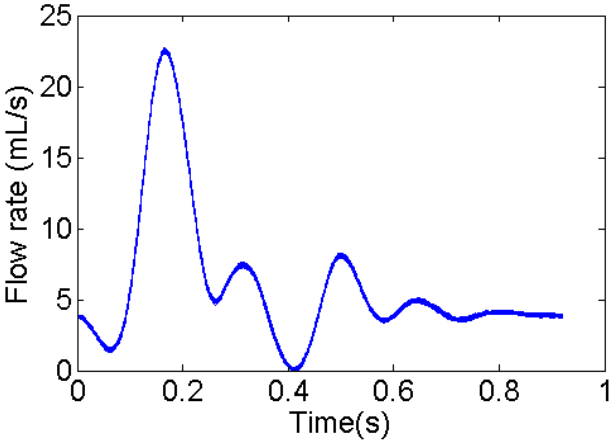

Figure A.3: All waveforms used in this study are averaged over 30 cardiac cycles, each of the 30 cardiac cycles is shown for the flow-rate waveform in the rigid 50% stenosed phantom measured at the CCA inlet.

Figure A.4 shows the pressure and flow-rate waveforms measured in the flow loop consisting of only resistive elements typically placed downstream from the ECA. Since the pressure is extremely high (>800mmHg) because of the small diameter tubing, the accuracy of the model parameter (R_{ed} and R_{id}) was in doubt. For this reason, the adjusted 'young' waveform with a peak of 5 and 10 mL/s was tested as well as the 'old' waveform. Identical parameter values were obtained for all these waveforms with much lower systolic pressure. The results are shown in Figure A.5 for the resistive elements typically downstream of the ICA and Figure A.6 for the resistive elements typically downstream of the ECA.

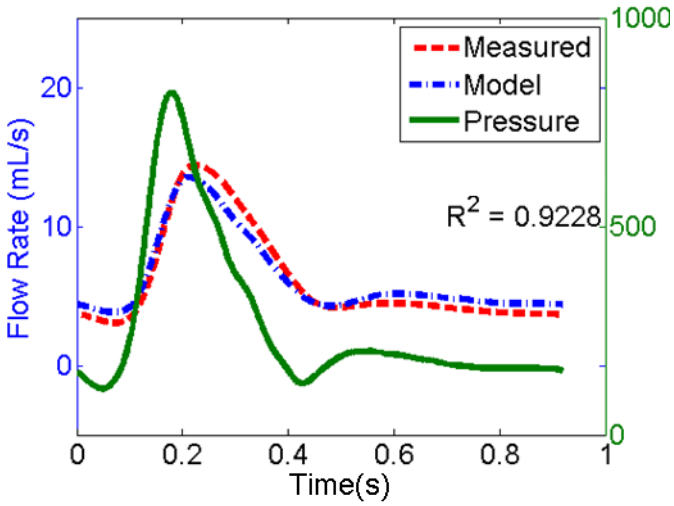

Figure A.4: The measured and modelled flow-rate waveform, and the pressure waveform (secondary axis) are shown for the flow loop consisting of only resistive elements typically placed downstream of the ECA.

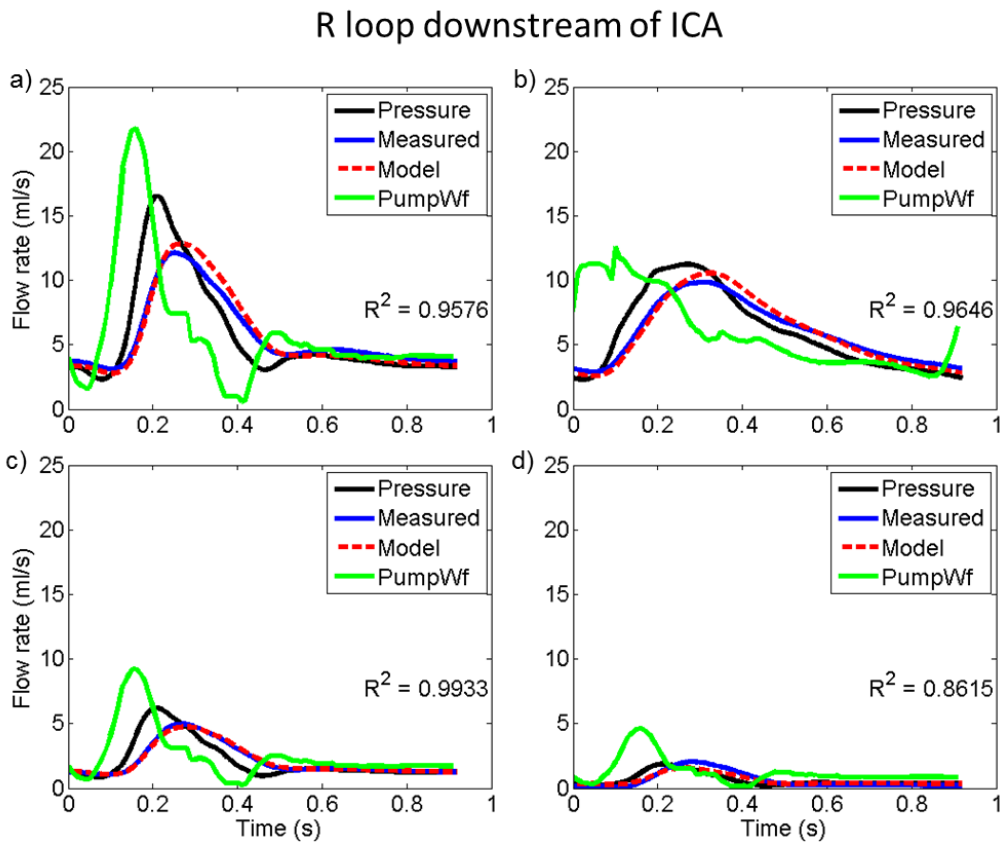

Figure A.5: The measured and modelled flow-rate waveforms, pump input waveforms and the pressure waveforms divided by the resistance of the loop are shown for the flow loop consisting of only resistive elements typically placed downstream of the ICA. The following waveforms are shown: (a) the 'young' adult waveform, (b) the 'old' adult waveform, (c) the peak of the 'young' adult waveform has been reduced to 10 mL/s and (d) the peak of the 'old' adult waveform has been reduced to 5 mL/s.

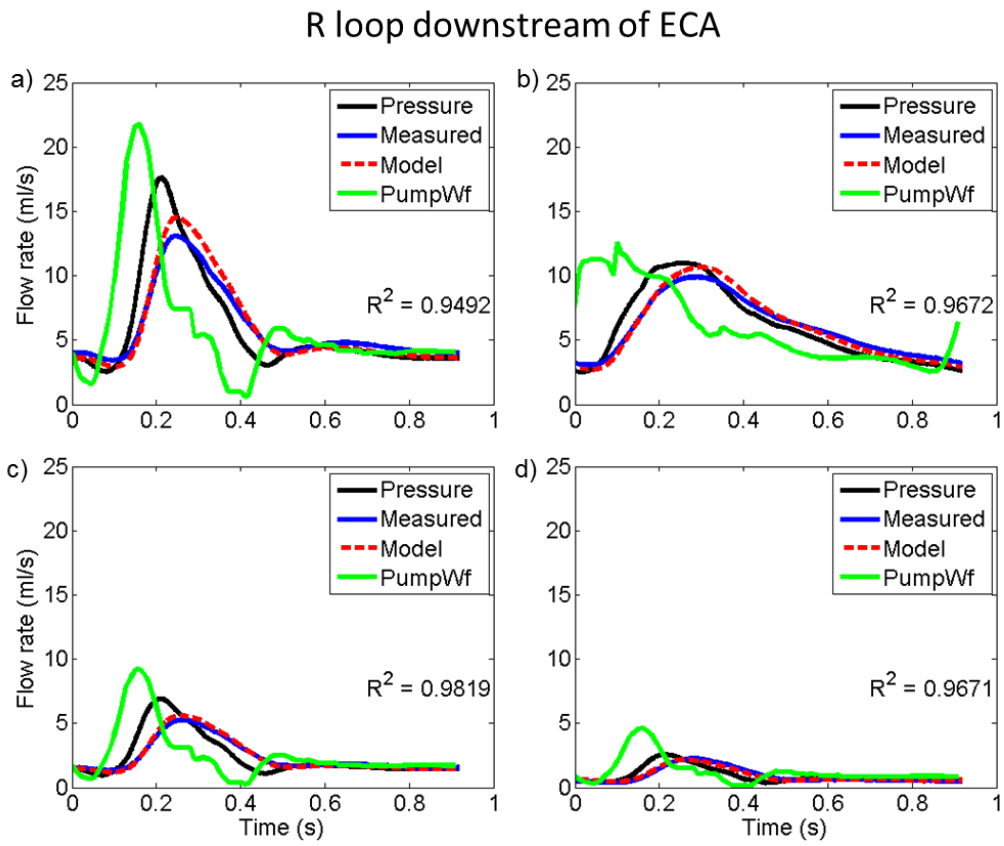

Figure A.6: The measured and modelled flow-rate waveforms, pump input waveforms and the pressure waveforms divided by the resistance of the loop are shown for the flow loop consisting of only resistive elements typically placed downstream of the ECA. The following waveforms are shown: (a) the 'young' adult waveform, (b) the 'old' adult waveform, (c) the peak of the 'young' adult waveform has been reduced to 10 mL/s and (d) the peak of the 'old' adult waveform has been reduced to 5 mL/s.

The effects of the inertance parameter is shown. A well-matched modelled flow-rate waveform cannot be obtained if the LP model contains no inertance term.

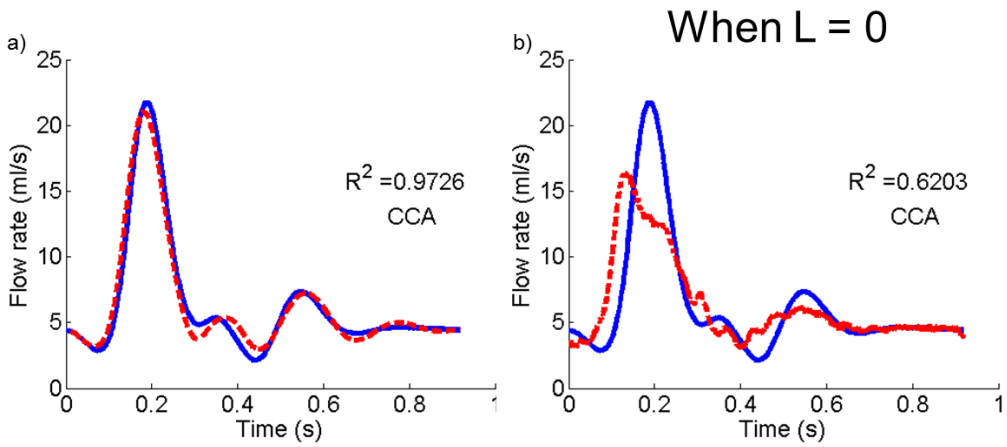

Figure A.7: Measured and modelled flow-rate waveforms are shown for the rigid 50% stenosed phantom at the inlet of the CCA. (a) The inertance (L_{ica}, L_{eca}) as listed in Table 2.1 are used. (b) The inertance (L_{ica}, L_{eca}) has been set to 0 and the modelled waveform no longer matches the measured waveform.

Appendix B

Impedance Plots for all phantoms and configurations

Figure B.1 shows the modulus of the impedance for the four phantoms with increasing resistance and Figure B.2 shows the phase of the impedance. The impedance is well-matched at the low frequencies but starts to deviate at higher frequencies.

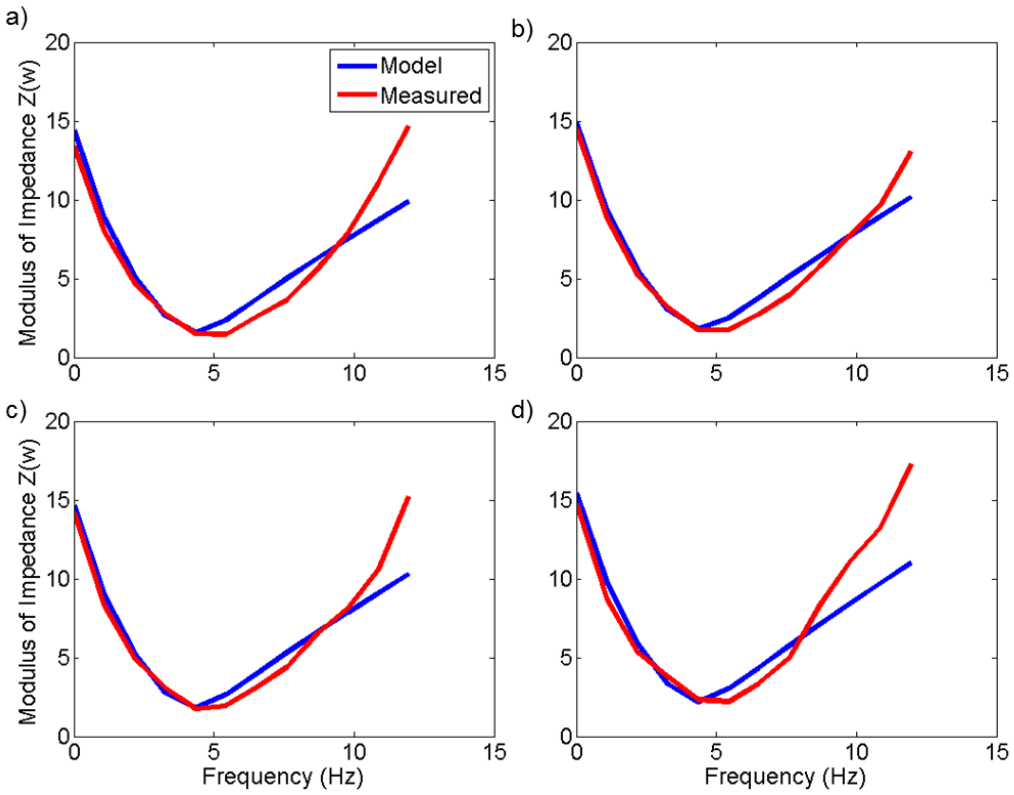

Figure B.1: The measured and calculated modulus of the impedance is shown for the rigid phantoms with increasing stenosis severity (a) no stenosis, (b) 30%, (c) 50% and (d) 70% stenosis. *NOTE: results for the compliant 50% phantoms are shown in Figure 2.6.

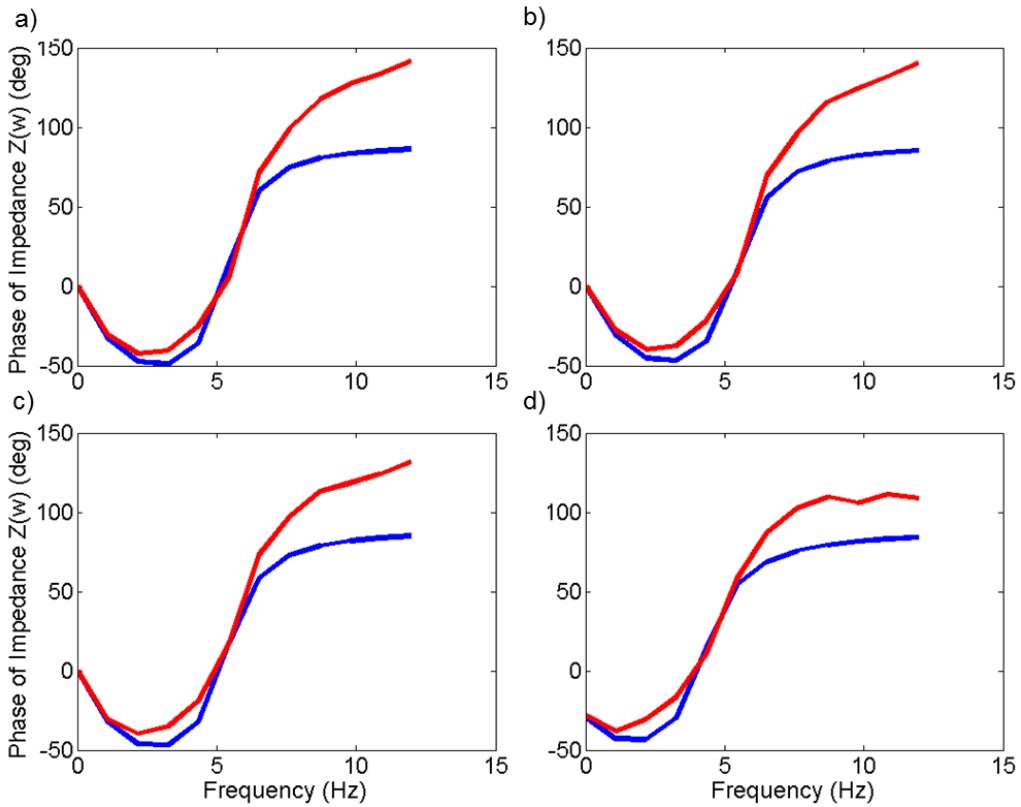

Figure B.2: The measured and calculated phase of the impedance is shown for the rigid phantoms with increasing stenosis severity (a) no stenosis, (b) 30%, (c) 50% and (d) 70% stenosis. *NOTE: results for the compliant 50% phantoms are shown in Figure 2.6.

Figure B.3 shows the modulus and impedance of the ICA (a,b) and ECA (c,d) outlets in the rigid 50% stenosed phantom. Modulus is extremely well-matched in this case but some deviations between measured and modelled phase of the impedance exist.

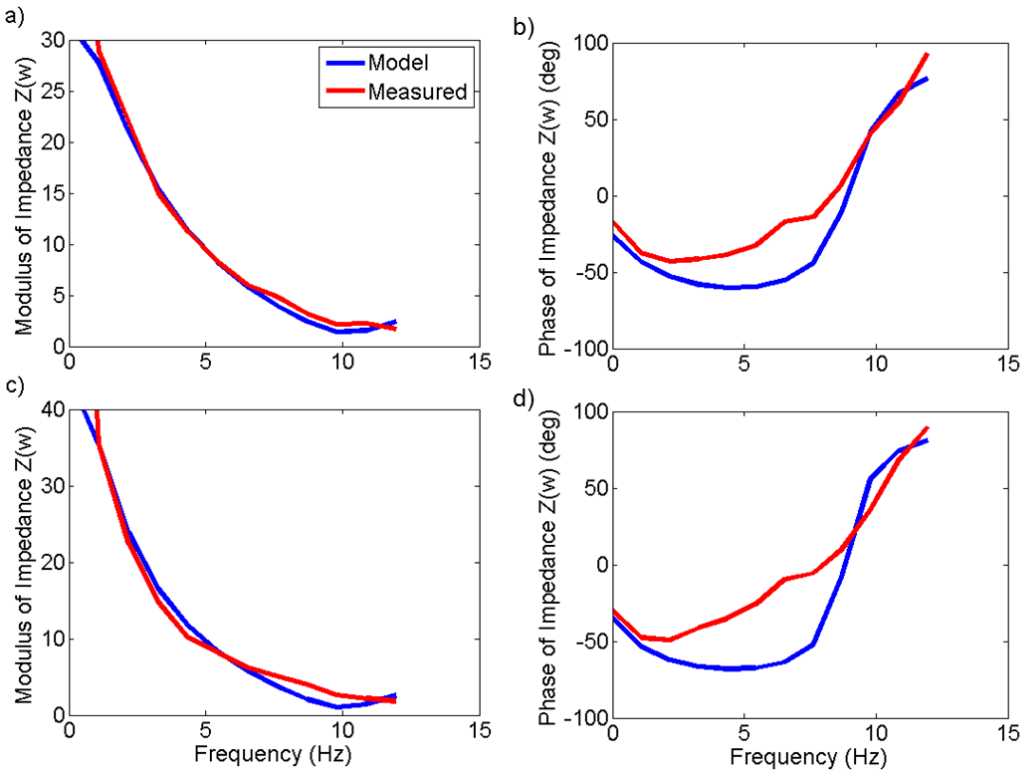

Figure B.3: The measured and calculated modulus (a,c) and phase (b,d) and of the impedance are shown for the rigid 50% stenosed phantoms at the outlets of the ICA (a,b) and ECA (c,d).

Appendix C

Pressure and Flow-rate waveforms (‘old’ waveform)

Figure C.1-7 show the supplementary data that were measured. It contains all the data for the ‘old’ waveform in the resistive only and resistive and compliant loop as well as the full phantom loops. The measured and modelled waveforms measured in the ICA and ECA outlets are also shown (both ‘young’ and ‘old’ waveforms).

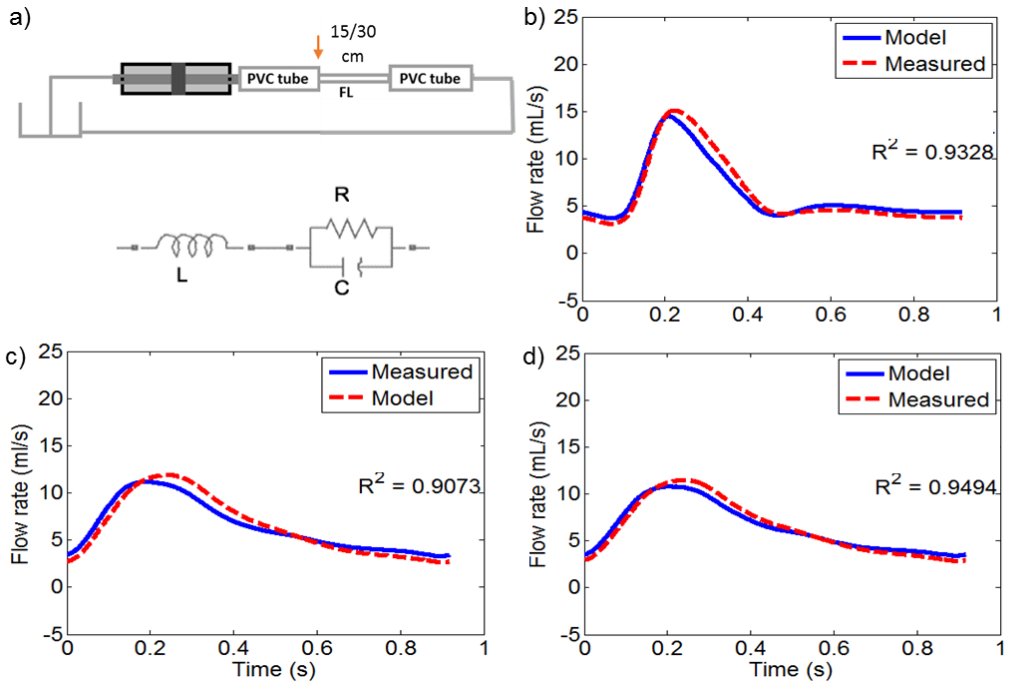

Figure C.1: The flow loop containing only resistive elements and the reduced R,L,C model are shown (a). Measured and modelled flow-rate waveforms representing ‘young’ (b) and ‘old’ (c,d) adults are shown. The results are shown for two reduced loop, one containing only the resistive elements typically placed downstream from the ICA (c) and the other typically placed downstream from the ECA (b,d). *NOTE: the ‘young’ waveform results measured in the reduced flow loop with resistive elements downstream from the ICA are shown in Figure 2.4a.

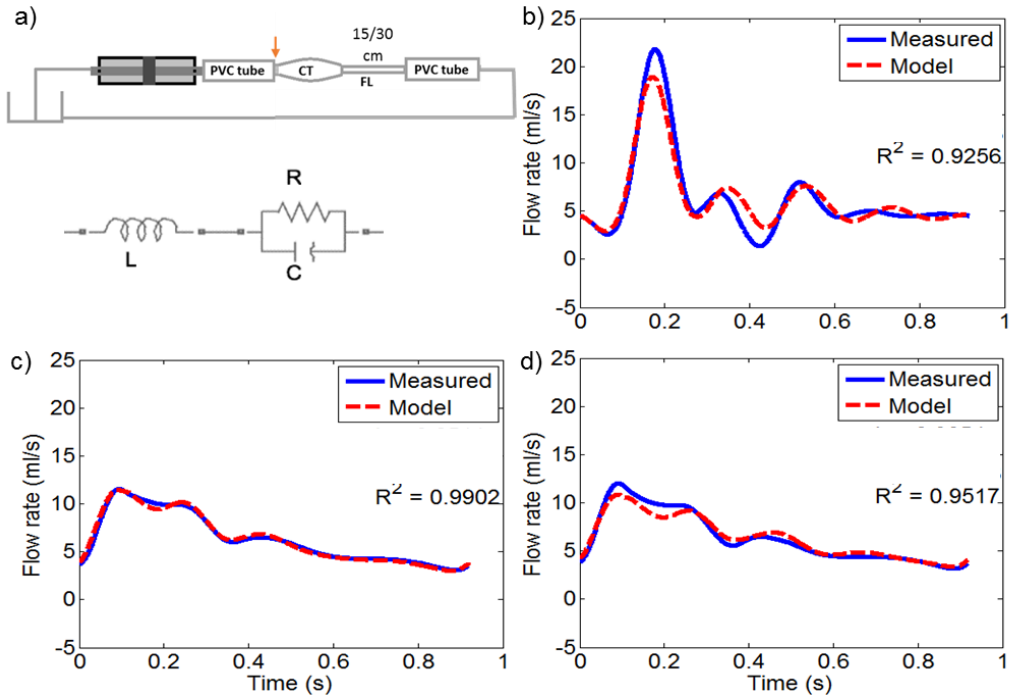

Figure C.2: The flow loop containing resistive and compliant elements and the reduced R,L,C model are shown (a). Measured and modelled flow-rate waveforms representing 'young' (b) and 'old' (c,d) adults are shown. The results are shown for two reduced loops containing resistive and compliant components, one typically placed downstream from the ICA (c) and the other typically placed downstream from the ECA (b,d). *NOTE: the 'young' waveform results measured in the reduced flow loop typically downstream from the ICA are shown in Figure 2.4b.

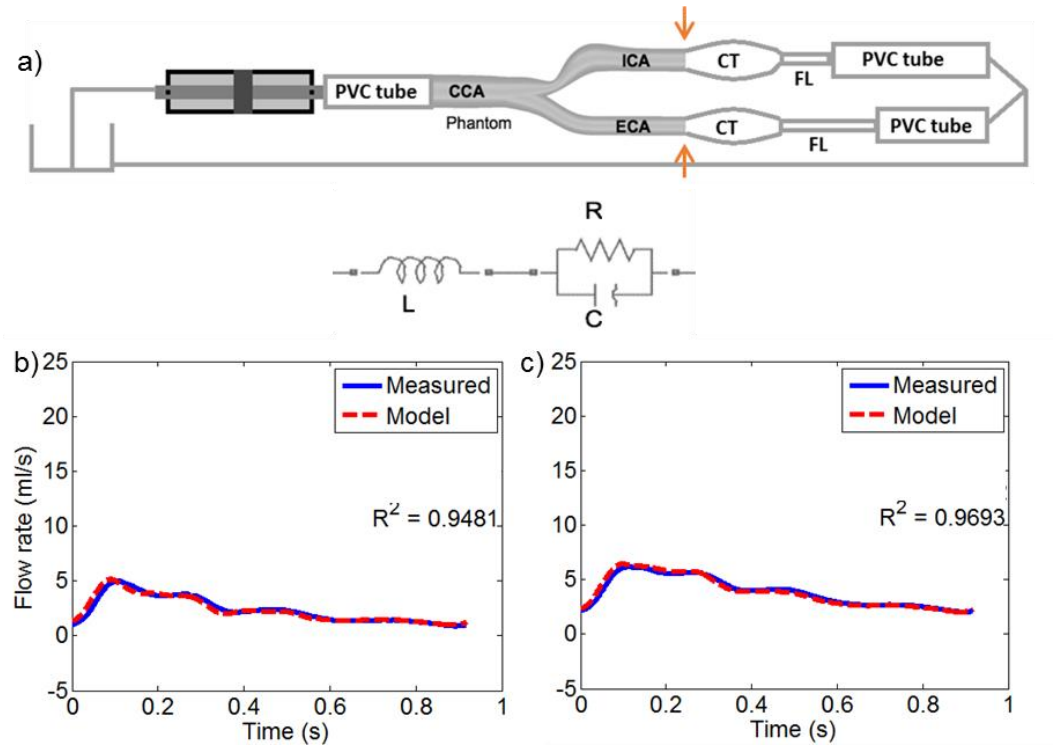

Figure C.3: In the full flow loop measurements are made at the outlets of ICA and ECA as indicated by the arrows and a reduced R,L,C model is used (a). Measured and modelled flow-rate waveforms representing 'old' (b,c) adults are shown for the rigid 50% stenosed phantom at the outlets of the ECA (b) and ICA (c). *NOTE: results for the 'young' waveforms are shown in Figure 2.4c.

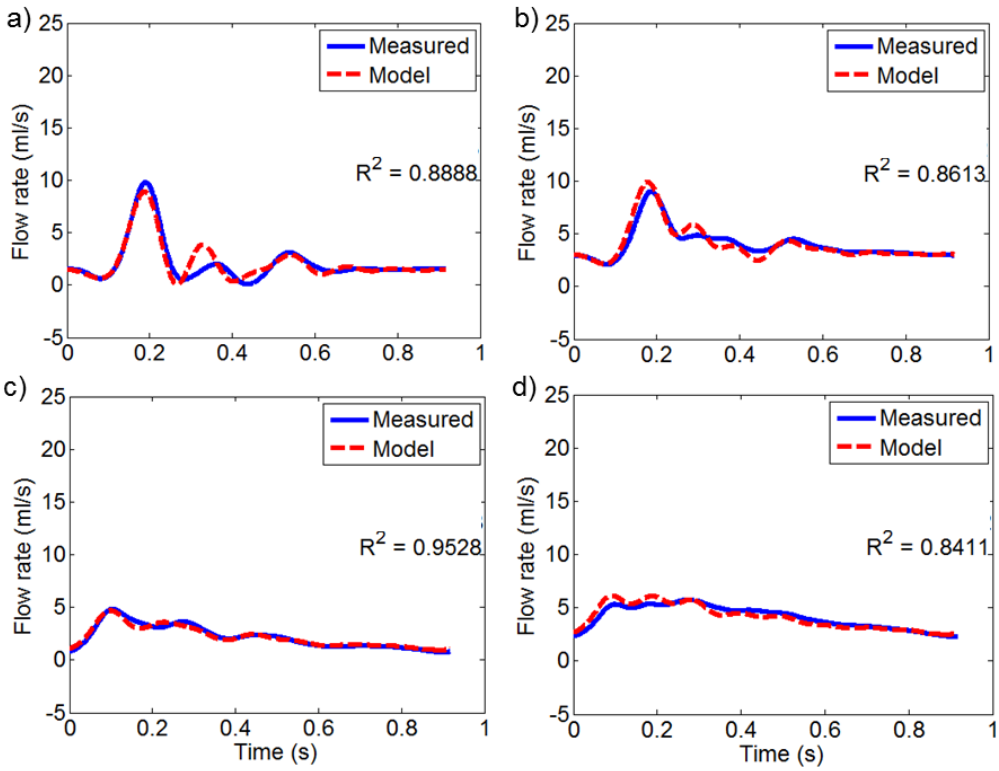

Figure C.4: Measured and modelled flow-rate waveforms in the compliant 50% stenosed phantom representing 'young' (a,b) and 'old' (c,d) adults measured at the outlets of the ECA (a,c) and ICA (b,d).

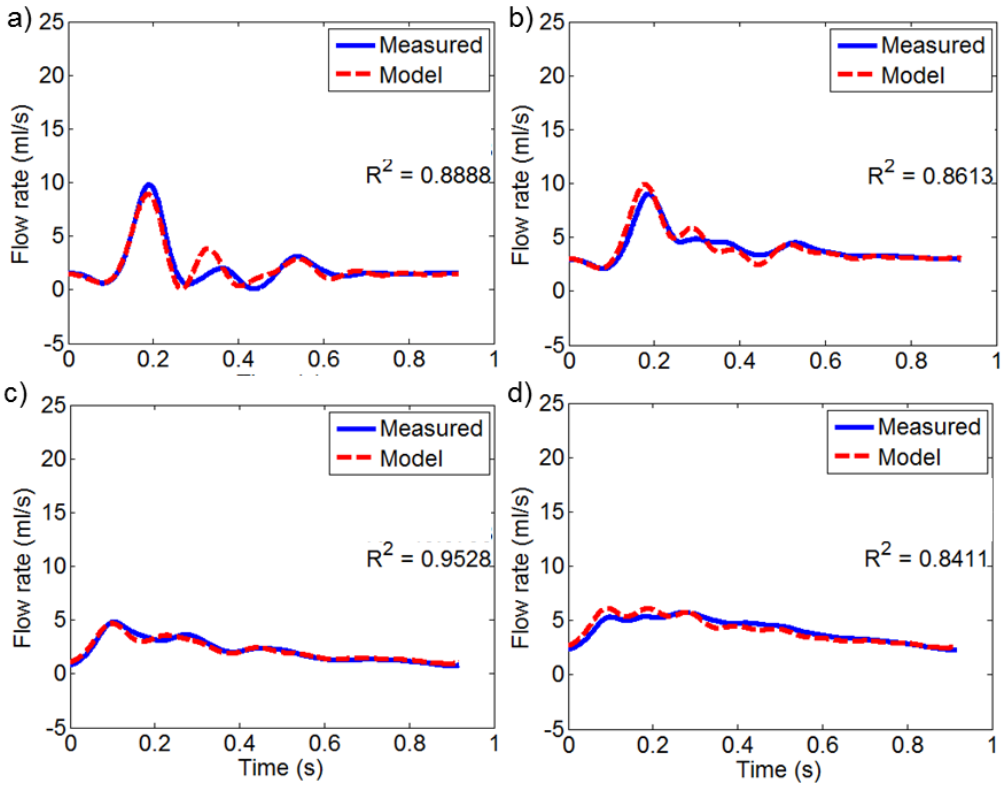

Figure C.5: Measured and modelled flow-rate waveforms in the rigid normal phantom representing 'young' (a,b) and 'old' (c,d) adults measured at the outlets of the ECA (a,c) and ICA (b,d).

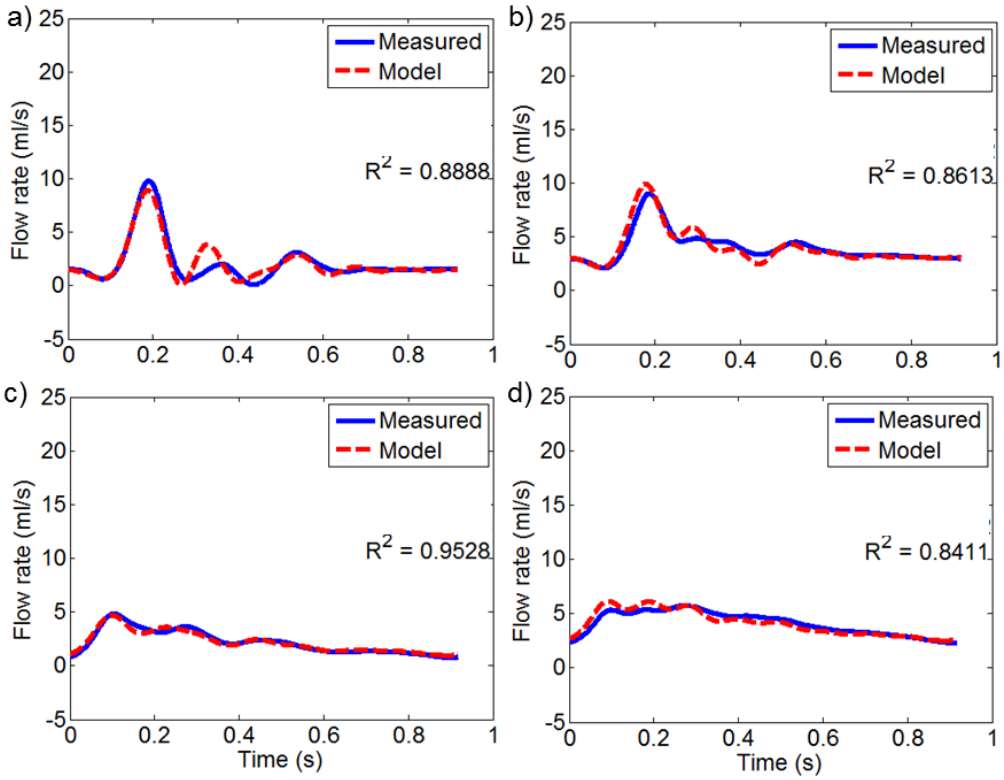

Figure C.6: Measured and modelled flow-rate waveforms in the rigid 30% stenosed phantom representing 'young' (a,b) and 'old' (c,d) adults measured at the outlets of the ECA (a,c) and ICA (b,d).

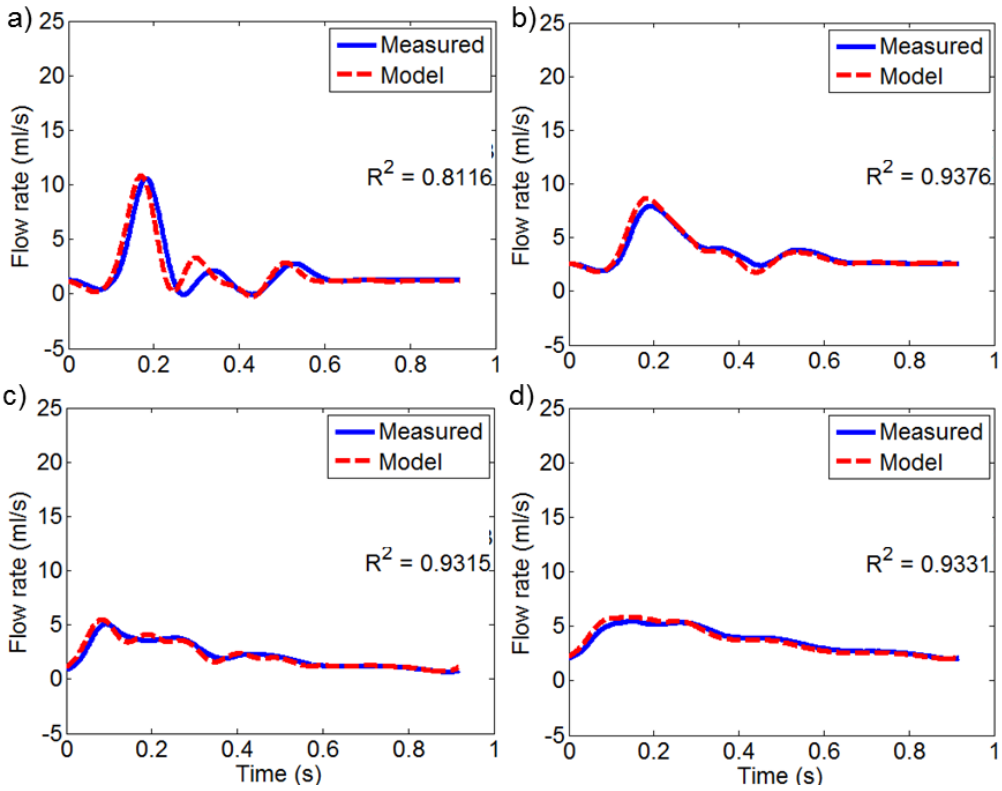

Figure C.7: Measured and modelled flow-rate waveforms in the rigid 70% stenosed phantom representing 'young' (a,b) and 'old' (c,d) adults measured at the outlets of the ECA (a,c) and ICA (b,d).

Figure C.8 shows the measured and modelled flow rate waveforms in the loop consisting of only resistive elements where the flow resistor has now been removed. As can be seen from the parameter values, the resistance has dropped significantly to 1.9 mmHg/(mL/s) whereas the typical resistance downstream from the ICA is 24.2 mmHg/(mL/s) and ECA is 38.5 mmHg/(mL/s). This means that flow resistors dominate the downstream resistance.

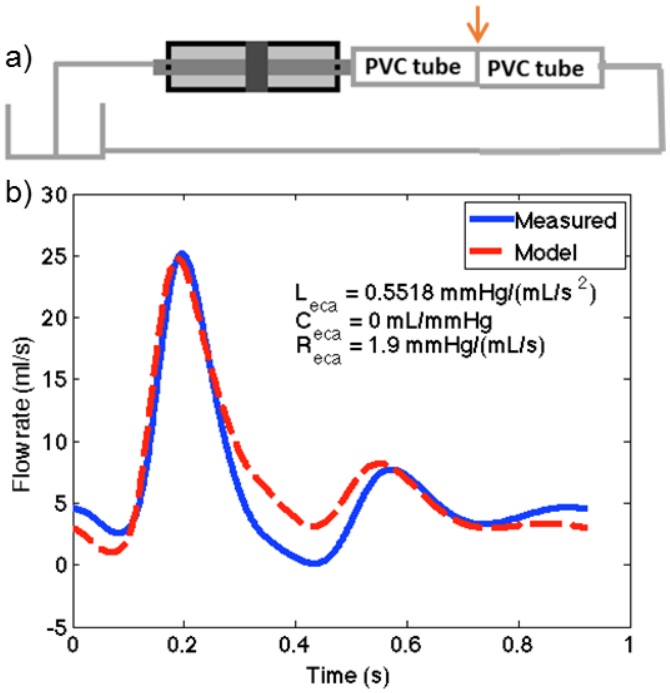

Figure C.8: (a) The flow loop containing all the rigid tubing that is typically placed downstream of flow resistor is used to obtain resistance values for the PVC tubing. (b) Measured and modelled flow-rate waveforms measured in the flow loop shown in part (a) at the location indicated by the arrow. *NOTE: in this figure different notation is used since it was one of the earliest figures designed: L_{eca} actually represents L_{ed}, C_{eca} represents C_{ed} and R_{eca} represents R_{ed}.

Figure C.9 shows the measured and modelled flow-rate waveforms representing the 'young' and 'old' adults in the compliant 50% stenosed phantom. The impedance is shown in Figure 2.6.

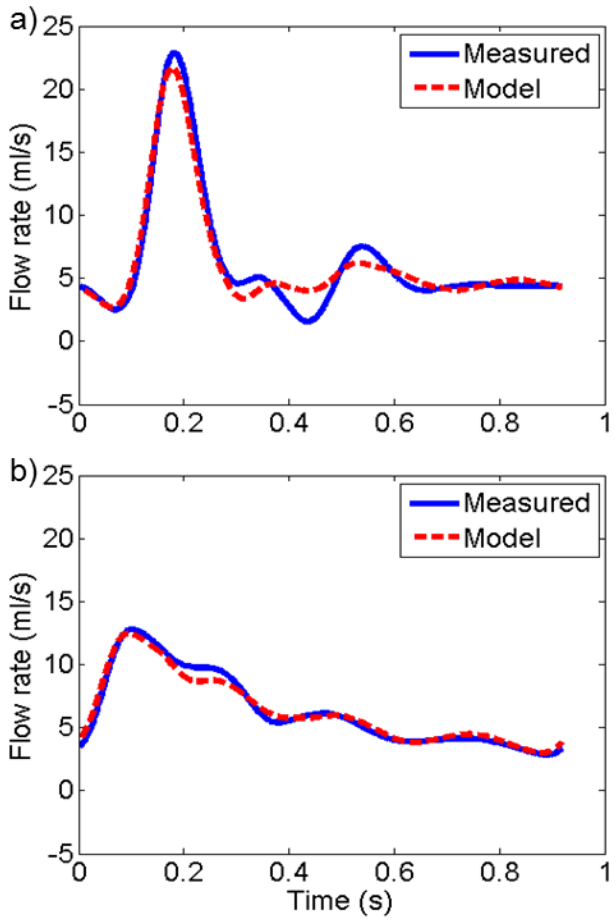

Figure C.9: Two measured and modelled flow-rate waveforms (R^2 > 0.96) at the CCA inlet of the compliant 50% stenosed phantom representing (a) 'young' and (c) 'old' adults.

Figure C.10 shows the CCA pressure waveforms with increasing resistance (R_{ica}) and compliance (C_{ica}, C_{eca}) representing the 'old' waveform.

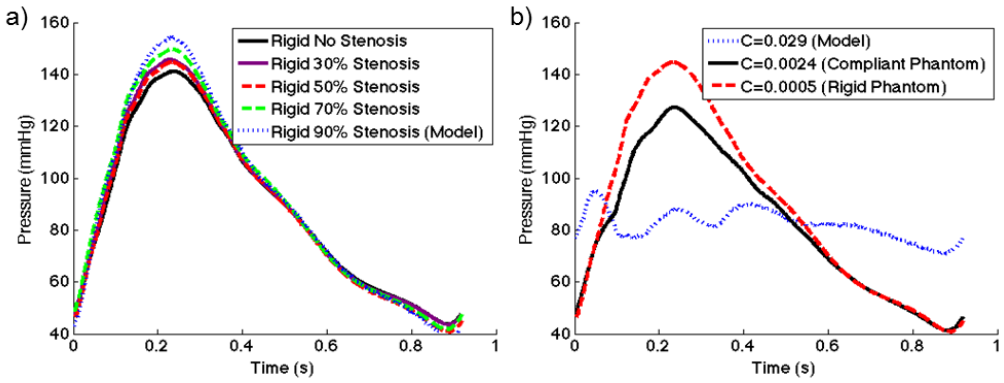

Figure C.10: Using the 'old' flow-rate waveform, measured CCA pressure waveforms with shown (a) increasing stenosis severity as well as the modelled case when R_{ica} is increased to 90% stenosis level, (b) increasing compliance as well as the modelled case when C_{ica} and C_{eca} are increased to physiological levels.

Appendix D

Expansion of Results

Figure D.1 shows the measured CCA inlet and ICA outlet flow-rate waveforms in the five different phantoms used in this study. Figure D.2 takes the mean ICA flow-rates and plots it against the diameter of the ICA stenosis to plot the exponential curve for comparison purposes. Figure D.3 shows the flow division (ratio of ICA/ECA flow-rate) through one cardiac cycle for the rigid 50% stenosed phantom. Figure D.4 shows the flow conservation (ICA + ECA)/CCA of the flow-rate for the rigid 50% stenosed phantom. A phase lag is observed in both the flow division and flow conservation figures.

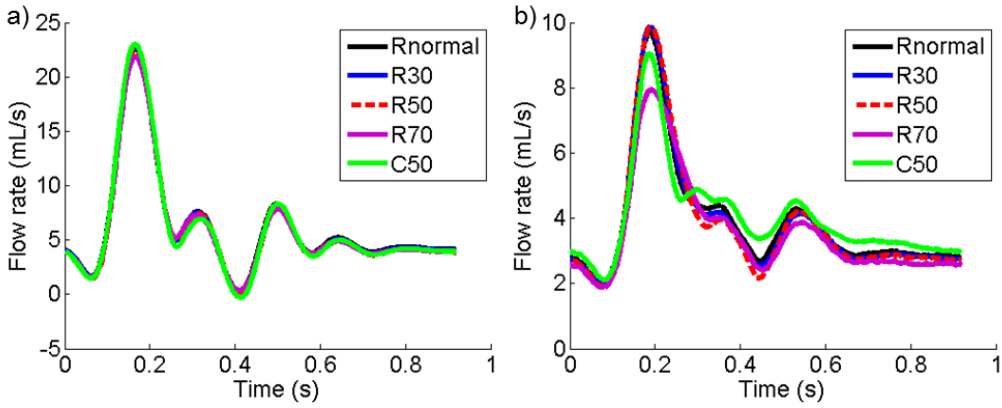

Figure D.1: Flow-rate waveforms for the five phantoms used in this study: rigid normal (Rnormal), rigid with 30% stenosis (R30), rigid 50% (R50), rigid 70% (R70) and compliant 50% (C50) are measured at the (a) CCA inlet and (b) ICA outlet.

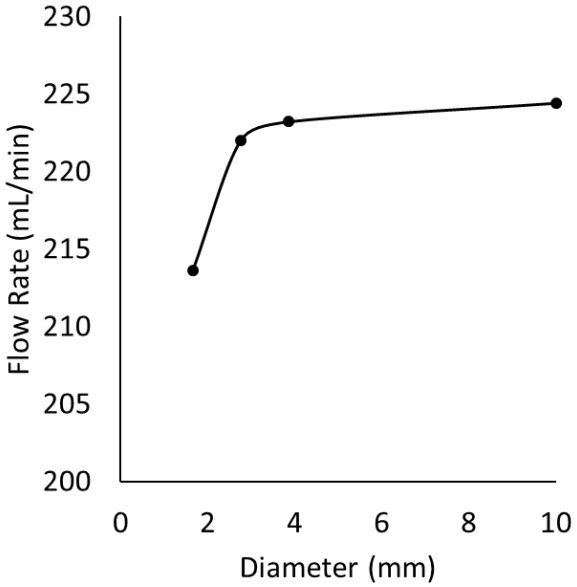

Figure D.2: Mean ICA flow-rate is plotted against the diameter of the stenosis.

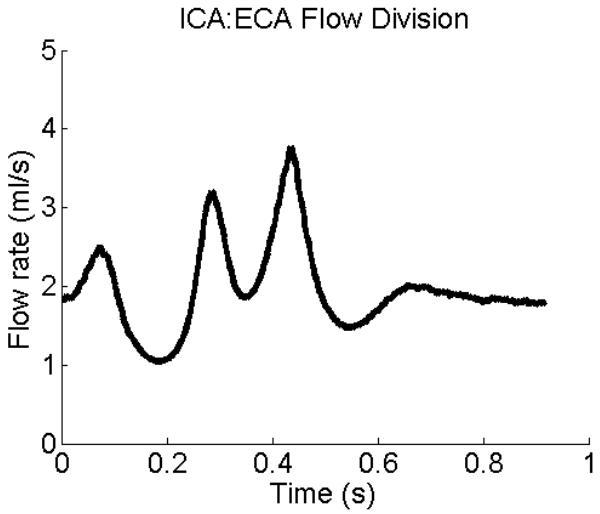

Figure D.3: Ratio of ICA/ECA flow-rate through one cardiac cycle in a rigid 50% stenosed phantom.

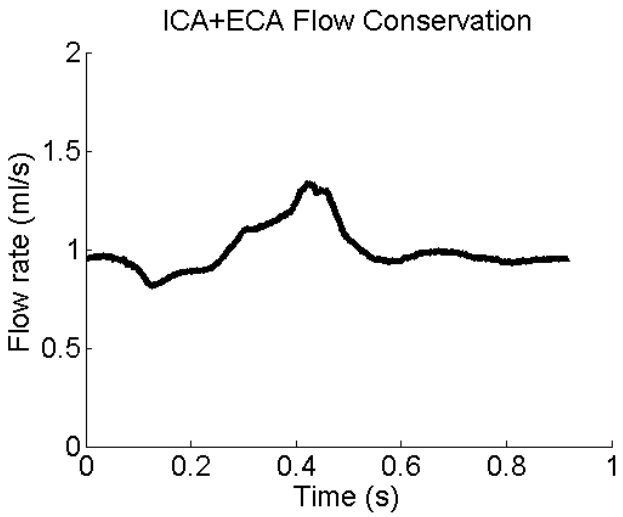

Figure D.4: The ratio of the sum of ICA and ECA flow-rate to the CCA flow-rate through one cardiac cycle in a rigid 50% stenosed phantom.

Figure D.5 shows the resistance (R_{ica}) as determined via the LP model plotted against the diameter of the stenosis. Also plotted is the predicted resistance via Poiseulle's Law (Eq. C.1, where r is the radius of the vessel, L is the length of the vessel and η is the viscosity of the fluid). This resistance deviates highly from the derived resistance which demonstrates why it is not an effective assumption in the arterial system.

$$R = \frac{8\eta L}{\pi r^4} \qquad \text{C.1}$$

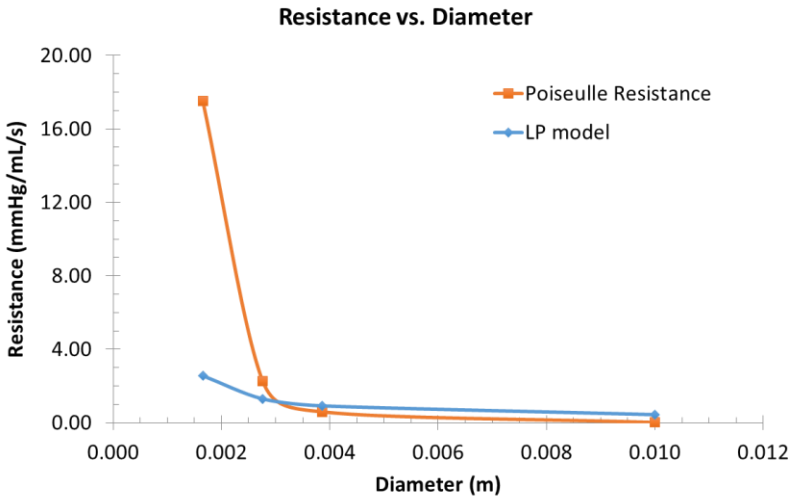

Figure D.5: The resistance parameter (R_{ica}) as determined through iteratively matching waveforms by use of the LP model is plotted against the diameter of the stenosis. Also, plotted is the resistance obtained through Poiseuille's Law.

Figure D.6 shows the measured CCA flow-rate waveforms in the four rigid phantoms with increasing stenosis and the predicted CCA pressure waveform if resistance is increased to downstream levels. As can be seen, the pressure waveform changes dramatically with a drastic increase in systolic blood pressure.

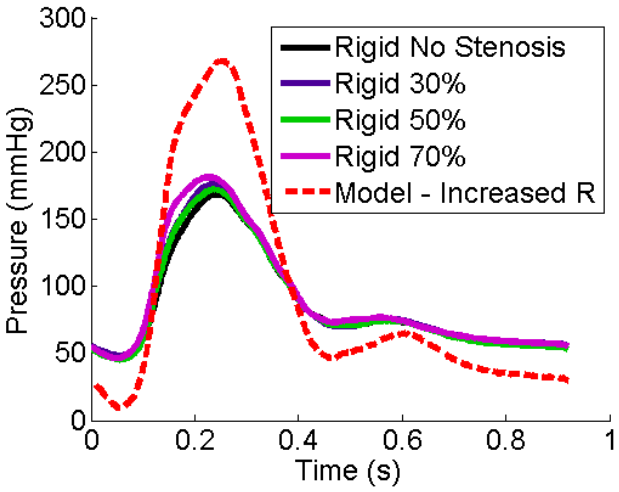

Figure D.6: When the resistance (R_{ica}) is significantly increased such that it is comparable to downstream levels.

Figure D.7 demonstrates potential results if the system was pressure-controlled instead of CCA flow-controlled. Often, pressure is regulated in vivo through the carotid baroreceptors and changes in flow-rate are more probable. If the pressure waveform remains fixed, increasing resistance due to stenosis (R_{ica}) results in a decrease in flow-rate.

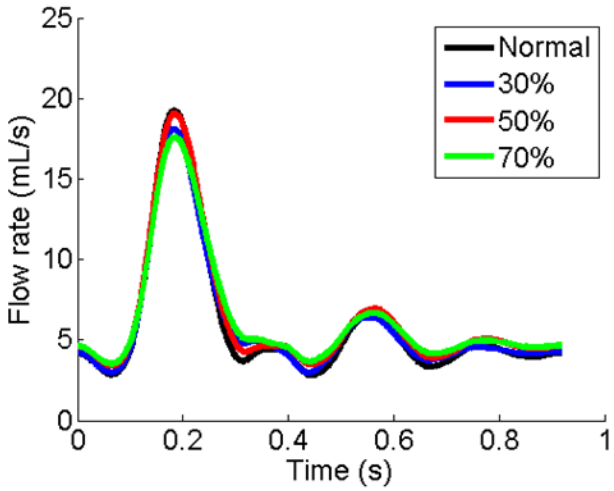

Figure D.7: The predicted flow-rate waveforms from the rigid phantoms with increasing stenosis if the pressure waveform is kept constant.

Curriculum Vitae

Name:	Onaizah Onaizah
Post-secondary Education and Degrees:	University of Toronto Toronto, Ontario, Canada 2009-2013 Honours' B.Sc. The University of Western Ontario London, Ontario, Canada 2013-2015 M.Sc.
Honours and Awards:	CIHR STP Fellowship in Vascular Research ($24,000) 2013-2015 Western Graduate Research Scholarship ($9,000) 2013-2015
Related Work Experience	Graduate Research Assistant The University of Western Ontario 2013-2015

Publications:

Onaizah, O., T. L. Poepping, M. Zamir. (2015) Effects of Carotid Artery Disease on Blood Supply to the Brain: Theoretical and Experimental Study. Submitted to the *Journal of Biomechanics*.

Onaizah, O., Poepping, T.L., and Zamir, M. (2015) Obstructive vs Sclerotic Disorders affecting Carotid Blood Flow to the Brain. *World Congress of Medical Physics and Biomedical Engineering*.

Onaizah, O., Poepping, T.L., and Zamir, M. (2015) Lumped Parameter Model of Flow through the Carotid Bifurcation. *25th Canadian Congress of Applied Mechanics*.

Poepping, T.L., DiCarlo, A., **Onaizah, O.**, and Zamir, M. (2015) Evaluating Flow Disturbances in the Carotid Bifurcation. *25th Canadian Congress of Applied Mechanics*.

Oral Presentations:

Onaizah, O., Poepping, T.L., and Zamir, M. (2015) Lumped Parameter Model of Flow through the Carotid Bifurcation. Oral Presentation at: *25th Canadian Congress of Applied Mechanics*.

Onaizah, O., Poepping, T.L., and Zamir, M. (2014) Lumped Parameter Model of Flow through the Carotid Bifurcation. Oral Presentation at: *9th London Imaging Discovery Day*.

Onaizah, O., Poepping, T.L., and Zamir, M. (2014) Blood Flow to the Brain. Oral Presentation at: *Three Minute Thesis competition*.

Poster Presentations:

Onaizah, O., Poepping, T.L., and Zamir, M. (2015) Obstructive vs Sclerotic Disorders Affecting Carotid Blood Flow to the Brain. Poster presented at: *World Congress of Medical Physics and Biomedical Engineering*.

Onaizah, O., Poepping, T.L., and Zamir, M. (2015) Obstructive vs Sclerotic Disorders Affecting Carotid Blood Flow to the Brain. Poster presented at: *13th Imaging Network Ontario Symposium*. **1st Place Poster Prize!**

Onaizah, O., Poepping, T.L., and Zamir, M. (2015) Obstructive vs Sclerotic Disorders Affecting Carotid Blood Flow to the Brain. Poster presented at: *London Health Research Day*.

Onaizah, O., Poepping, T.L., and Zamir, M. (2014) Lumped Parameter Model of Flow through the Carotid Bifurcation. Poster presented at: *Western Interdisciplinary Science Research Showcase*.

Onaizah, O., Poepping, T.L., and Zamir, M. (2014) Lumped Parameter Model of Flow through the Carotid Bifurcation. Poster presented at: *9th London Imaging Discovery Day*.

Onaizah, O., Poepping, T.L., and Zamir, M. (2014) Modified Windkessel Model (MWM) of the Carotid Bifurcation. Poster presented at: *London Health Research Day*.

Onaizah, O., Kolonjari, F., Waymark, C., and Walker, K. (2013) Validation of ACE-FTS with ozonesonde measurements. Poster presented at: *NSERC CREATE Summer School in Arctic Atmospheric Science*. Abstract online.